

# Phononic simulation and detection in a trapped ion system

Harry Parke





# Phononic simulation and detection in a trapped ion system

Harry Parke

Academic dissertation for the Degree of Doctor of Philosophy in Physics at Stockholm University to be publicly defended on Tuesday 26 May 2026 at 10.00 in hörsal 6, hus 4, Albano, Albanovägen 12.

## Abstract

Trapped ion systems are at the forefront of the development of various forms of quantum technology. Continuing to improve and establish new devices and techniques for the control of trapped ions is a vital element of ongoing research. In this thesis, a range of experiments which aim to expand the quantum toolkit of trapped ion systems are presented. These results primarily focus on the control and detection of bound motional states of a single trapped  $^{88}\text{Sr}^+$  ion for the purposes of quantum simulation and computation. We demonstrate how the interference between motional modes can reveal an interesting new interpretation of the mechanism behind light-matter interaction and introduce two separate techniques for the detection of motional states, based on the Autler-Townes effect and the use of composite pulses respectively. Additionally, we introduce a novel method to perform micromotion compensation and build upon previous works studying the effects of trapping electric fields on a single trapped Rydberg ion, observing the second-order quadrupolar response of the ion with a highly precise sensitivity.

**Keywords:** *Quantum technology, Optics, Atomic physics, phonons, ion trapping, Rydberg ions.*

Stockholm 2026

<http://urn.kb.se/resolve?urn=urn:nbn:se:su:diva-254102>

ISBN 978-91-8107-588-5  
ISBN 978-91-8107-589-2

Department of Physics

Stockholm University, 106 91 Stockholm





PHONONIC SIMULATION AND DETECTION IN A TRAPPED ION  
SYSTEM

Harry Parke





# Phononic simulation and detection in a trapped ion system

Harry Parke

©Harry Parke, Stockholm University 2026

ISBN print 978-91-8107-588-5

ISBN PDF 978-91-8107-589-2

Printed in Sweden by Universitetservice US-AB, Stockholm 2026

## Sammanfattning

---

Experimentella system med fångade joner är banbrytande i utvecklingen av olika former av kvantteknologi. Att ständigt förbättra och skapa nya enheter och tekniker för kontroll av fångade joner är en väsentlig del av pågående forskning. I den här avhandlingen presenteras ett urval av experiment med målet att utvidga de tillgängliga verktygen som ett system av fångade joner använder sig av. De här resultaten fokuserar främst på hur en enda  $^{88}\text{Sr}^+$  jons bunda rörelsetillstånd kan kontrolleras och verifieras. Vi demonstrerar hur interferens mellan rörelsetillstånd avslöjar en intressant ny tolkning på det underliggande fenomenet bakom interaktionen mellan ljus och materia. Vi introducerar också två nya metoder för att mäta rörelsetillstånd. Dessutom presenterar vi en ny teknik som används för att minska oönskad rörelse i systemet. Slutligen visar vi resultat som är en fortsättning av tidigare experiment bestående av studier om hur en fångade Rydberg jon interagerar med det fångande elektriska fältet. I det här fallet observerar vi effekter som härstämmer från jonens kvadrupolär polariserbarhet.

## Abstract

---

Trapped ion systems are at the forefront of the development of various forms of quantum technology. Continuing to improve and establish new devices and techniques for the control of trapped ions is a vital element of ongoing research. In this thesis, a range of experiments which aim to expand the quantum toolkit of trapped ion systems are presented. These results primarily focus on the control and detection of bound motional states of a single trapped  $^{88}\text{Sr}^+$  ion for the purposes of quantum simulation and computation. We demonstrate how the interference between motional modes can reveal an interesting new interpretation of the mechanism behind light-matter interaction and introduce two separate techniques for the detection of motional states, based on the Autler-Townes effect and the use of composite pulses respectively. Additionally, we introduce a novel method to perform micromotion compensation and build upon previous works studying the effects of trapping electric fields on a single trapped Rydberg ion, observing the second-order quadrupolar response of the ion with a highly precise sensitivity.

## Acknowledgments

---

To begin with I would like to give a huge thank you to my supervisor Markus Henrich, your guidance, perpetual positivity, insight and encouragement were the backbone on which this PhD work was supported. To my assistant supervisor Ana, I would like to thank you for your support at every stage, your technical knowledge and many wisdoms have been invaluable inside and out of the lab. I would also like to give a special thanks to both as I approach the final hurdle, Markus for your limitless patience during my time in the group and Ana for your more limited patience in the time since, I wouldn't have gotten this far without either.

I would like to thank my former colleagues, Gerard, Fabian and Chi for putting together such an impressive experiment and for always being helpful, understanding and enthusiastic in the lab. To learn from you all and see all that you managed to achieve was an inspiration to me. Thank you to all those who I shared time with in the lab over the years: Anders, Erik, Ivo, Simon, Luca and Tommaso. A huge thank you to our many South American visitors at the department: to Murilo, Alan, André, Fernando and Andrea. I enjoyed our many fruitful discussions at work and many fruitless discussions at afterworks and appreciate the time spent with you all. Thank you to Celso Villas-Boas, Romain Bachelard and Weibin Li for your theoretical collaboration over the years. There is a long list of people who helped to make Albanova such an enjoyable place to work so thank you to Ricardo, Jaewon, Ashraf, Emil, Junior, Thomas and to many others who came and went during my lengthy stay.

A huge thank you to WACQT for providing me the opportunity to do this work and for the many conferences, trips and lectures that I was lucky enough to attend. Being a part of the WACQT community, visiting so many interesting places and meeting so many interesting people across Sweden, was a highlight of my time during the PhD. A special thank you to my former WACQT colleague and good friend Alban, who accompanied me on many such trips, and made each and every one of them unforgettable (for better or worse).

My sincerest gratitude to all past and present members of the trapped Rydberg ion group: to Marion, who is as productive as anyone I have ever worked with and without whom many experiments would have taken much longer to succeed, to Robin, who I thoroughly enjoyed working closely with in the lab and whose knowledge and infectious optimism provided a solution to almost every problem, to Natalia, whose bright presence in the department made it a more enjoyable place to work for all and to whom I would turn to every day for help, inspiration and camaraderie, and to Shalina, who started out with me on day one of the PhD and

in whom I found endless support, whether it be discussing quantum mechanics, building optical systems, teaching lab courses or simply talking as friends.

Thank you to my family and in particular to my partner Anni, who was always there, ready with a smile, to comfort my worry or cheer my success. You encouraged me at the start, believed in me at the end, and filled every day between with support, love and joy. And finally to June, whose arrival somewhat delayed the publication of this thesis, but to whom I dedicate my whole world, one single atom at a time.

# Contents

<b>1</b>	<b>Introduction</b>	<b>1</b>
1.1	Included publications . . . . .	4
1.1.1	Publication I . . . . .	4
1.1.2	Publication II . . . . .	6
1.1.3	Publication III . . . . .	6
1.1.4	Publication IV . . . . .	7
1.1.5	Publication V . . . . .	7
<b>2</b>	<b>Theoretical background</b>	<b>8</b>
2.1	Ion trapping . . . . .	8
2.2	Bounded motional states . . . . .	11
2.2.1	Fock states . . . . .	11
2.2.2	Thermal states . . . . .	12
2.2.3	Coherent states . . . . .	13
2.3	Atom-light interactions . . . . .	13
2.3.1	Resonant coupling to a free atom . . . . .	13
2.3.2	Off-resonant coupling . . . . .	17
2.3.3	Dressed-states and the AC Stark effect . . . . .	17
2.3.4	Autler-Townes effect . . . . .	20
2.3.5	Quadrupole transitions . . . . .	21
2.3.6	Ion-phonon coupling for a trapped ion . . . . .	21
2.3.7	Lamb-Dicke regime . . . . .	23
2.3.8	Jaynes-Cummings interactions . . . . .	25
2.3.9	Bichromatic fields . . . . .	25
2.4	Trapped Rydberg ions . . . . .	26
2.4.1	Rydberg ion properties . . . . .	26
2.4.2	Dipole interaction with electric fields . . . . .	27
2.4.3	Higher-order interaction with electric fields . . . . .	29
2.4.4	Rydberg state trapping potentials . . . . .	29
<b>3</b>	<b>Experimental system</b>	<b>34</b>
3.1	Linear Paul trap . . . . .	34
3.2	Laser systems . . . . .	37
<b>4</b>	<b>Phononic bright and dark states: Investigating multi-mode interference with a single trapped ion</b>	<b>41</b>

5	Single-shot measurements of phonon number states using the Autler-Townes effect	42
6	Motional-state analysis of a trapped ion by ultranarrowband composite pulses	43
7	Observation of second- and higher-order electric quadrupole interactions with an atomic ion	44
8	Micromotion minimization using Ramsey interferometry	45
9	Summary and outlook	46
	Bibliography	52



# 1 Introduction

---

The following chapter as well as chapters 2 and 3 are partially adapted from the author's licentiate thesis (defended January 2022). The introduction is expanded and largely reformulated. Certain sections of chapters 2 (theoretical background) and 3 (experimental setup) including figs 2.1 2.3, 3.2 and table 2.1 have also been updated in the context of this work.

Trapped ion systems are a natural candidate for the study of both individual and many-body quantum systems. The experimental study of individual atoms was long considered a fantasy after the development of quantum mechanics in the 1920s; in today's experiments a single charged particle can be confined for weeks at a time, loaded on demand and utilized in a wide variety of ways as a tool for both fundamental research and the development of cutting-edge quantum technologies. The ability to control and engineer individual quantum systems for specific purposes is now a standard for most ion trapping experiments and is a key feature in the field of quantum information processing, for which ion traps are one of the leading archetypes. This is also due to the fact that, as computational resources, ions offer huge advantages in terms of abundance and universality. Multiple ions can be trapped in a single device and can be cooled and readout with minimal disturbance to their configurable structure. In most trapped ion systems a single physical qubit is commonly defined by a pair of the ion's electronic energy states and transitions are driven by optical or microwave pulses. Multi-qubit operations can be realized by various means; typically utilizing the collective motional state of a crystallized chain of ions. This was the idea first proposed by Cirac and Zoller in 1995 [1] which formed the basis of a field that now involves dozens of research groups.

In the three decades since trapped ion systems have achieved numerous benchmarks in terms of quantum computation including single-qubit gate operations with fidelities of 99.99% [2], coherence times exceeding one hour [3] and two-qubit entanglement operations with fidelities of 99.94% [4]. Outside of computation,

trapped ions have also achieved state-of-the-art precision in the form of atomic clocks [5] and have demonstrated broad appeal as quantum-enhanced sensors, with systems of up to 150 ions being used to perform high-precision electric field sensing [6]. Even for single ions, extremely sensitive measurements of electric fields have been made by detecting displacements over a magnetic field gradient [7] and novel approaches to overcome the standard quantum limit have been presented [8]. The nature of trapped ion systems, including their high level of control and use of both bosonic motional and fermionic spin states, also makes them excellent tools for quantum simulation. Among other proposals [9, 10], studies have been conducted for simulations of a wide range of many-body systems [11], open-quantum systems [12] and various phenomena within quantum optics [10].

In many cases, the basic requirements of an ion trap experiment are the following: efficient cooling, well-compensated excess micromotion, stable and well-defined atomic transitions, stable trapping frequencies and accurate detection methods for electronic and motional states. Given that the very first ion traps were developed in the 1950s [13], there exists a wide range of established techniques to meet these basic requirements. However, as the experiments which are performed continue to grow in complexity the development of faster, more accurate and more broadly applicable techniques is increasingly valuable. Maintaining a suitably-high fidelity whilst minimizing the timescale over which operations are performed is especially advantageous in quantum information processing considering the typically large number of operations required for such a device to outperform any classical machine [14]. Although purely technological advancements, for example in the design and function of lasers, electronic components, control software, etc., are necessary to drive the development of state-of-the-art ion trap systems, improved quantum toolkits based on novel techniques are invaluable to progress towards truly scalable quantum devices. Examples of such advancements can be seen in recent demonstrations of ion cooling based on electromagnetically-induced transparency [15], buffer gas collisions [16] and same-species sympathetic cooling [17]. In addition, new methods of qubit control which aim to reduce the complexity of future ion-trap based quantum information processors [18–20] are all exciting areas of research.

A trapped ion inherently offers the opportunity to utilize different types of quantum systems. Typically, experiments are performed with a discrete quantum system realized by the energy levels of the ion, where qubit states are defined between any pair of sufficiently long-lived states. At the same time, the quantized harmonic motion of the ion, which occurs as a consequence of its dynamic confinement, provides access to an entirely different kind of quantum system. Depending on the experimental conditions they can be strongly or weakly coupled, with a typical system operating in a regime where the two systems are almost completely

independent unless an interaction is mediated by an external light field. The temporary coupling of motional and electronic states has been the key component of most multi-qubit entangling operations demonstrated thus far [1, 21–23]. Recently however, trapped ion motion has seen increasing development as a powerful resource in and of itself, beyond simply the mediation of entanglement generation between electronic states. Phononic operations within trapped ion systems have been used to perform studies of bosonic arithmetic [24] and sub-universal computational networks [25]. In this thesis phononic operations are applied in a simulation of atom-cavity dynamics to provide insight into the mechanism behind light-matter interaction. As well as this, two novel techniques for the detection of an ion’s motional state are presented. The results provided by these works should enable even deeper study into the use of phonons in a variety of quantum computation and simulation experiments.

As with other paths towards viable quantum computation and other research areas involving trapped ions, the aforementioned phonon-mediated gate schemes, which are typical of many ion trap experiments, are currently limited in their scalability. Generally, a limit on the number of interconnected, uniquely-addressable qubits places an upper limit on the utility of the quantum device. This issue is compounded by the requirements of fault-tolerant computation; advancement beyond the current noisy intermediate-scale era of quantum computation (NISQ) will almost certainly be governed by the implementation of error-correcting codes [26–28] in order to overcome the limited fidelities of multi-qubit operations. Such schemes typically require a significant overhead in the number of operational qubits and although proof-of-principle implementations have already been demonstrated in trapped ion systems [29–34], large-scale fault tolerance poses a significant challenge. Similar issues stem from the fact that an  $N$  ion string has  $3N$  motional modes and gates which rely on the excitation of a particular mode(s) will suffer from spectral crowding as the number of ions is increased. Unwanted coupling to other motional modes will limit gate performance unless longer pulses can be used to improve the spectral resolution but this in turn limits the gate speed [35]. As a result, most gate schemes would benefit from qubits being broken up into isolated chains with a selective connectivity between them. Scalability has therefore become the central focus of many research groups. Different paths towards this goal have been proposed, including modular designs of micro-fabricated ion traps [36–39], photonic interfaces [40–42] and motional-mode engineering [43].

The use of Rydberg states to implement direct interactions between ions was proposed by Müller et al. in 2008 as one method to bypass the scaling issue [44]. The idea was to merge the advantageous elements of an ion trap quantum computer, such as the long coherence times and excellent qubit control, with the strong electronic interactions exhibited by Rydberg atoms. For neutral atoms arrays var-

ious well-established techniques exist in the the use of Rydberg states to entangle qubits [45–47] and these systems have the advantage that fast gate operations can be performed with only van der Waals interactions between Rydberg atoms. The strong, long-range interactions have enabled two-qubit entanglement operations to be performed with fidelities up to 99.5% [48] and for the generation of Greenberger-Horne-Zeilinger states of up to 20 qubits [49]. In the case of Rydberg ions, induced dipole-dipole coupling through the use of microwave dressing is required to realise a sufficiently strong interaction. Despite this, systems of trapped Rydberg ions have shown significant promise in their capability to implement fast entangling gates, most notably in the demonstration of a 700ns two-qubit phase gate with 78% fidelity [50]. For a trapped ion system the sub-microsecond gate time is significantly faster than a typical entangling gate but the fidelity is far from what would be required to work with error-correction schemes [51].

A trapped Rydberg ion also offers unique possibilities to study quantum phenomena that are inaccessible in neutral atom experiments. This is because the state-dependent trapping experienced by the ion in the Rydberg state does not necessarily force the ion out of the trap, as is often the case for systems of optical dipole traps which typically need to be switched off during Rydberg excitation to reduce atom loss [52]. Previous work at both Mainz University [53] and Stockholm University [54, 55] has aimed to characterise the unique system by studying how the properties of the Rydberg ion are affected by the strong electric fields that keep it confined. The goal of these experiments is carried forward in the study of Rydberg ion quadrupole polarisabilities that forms a part of this thesis.

## 1.1 Included publications

Below is a list of the five publications included in this thesis, including my individual contribution to each of the experiments.

### 1.1.1 Publication I

*Phononic bright and dark states: Investigating multi-mode interference with a single trapped ion.* Harry Parke, Robin Thomm, Alan Santos, André Cidrim, Gerard Higgins, Marion Mallweger, Natalia Kuk, Shalina Salim, Romain Bachelard, Celso Jorge Villas-Boas, Markus Hennrich. arXiv:2403.07154 (2024). Submitted to npj Quantum Information.

My contributions to this work are:

- I, along with Robin Thomm, carried out all of the measurements to observe

interference effects with bright and dark phononic states.

- I initially developed and tested two different schemes to prepare and observe bright and dark states with a single phonon. I implemented and optimized the scheme that was used to obtain the final results included in the manuscript.
- Robin and I made the necessary changes to our experimental system to allow us to generate coherent motional states for the first time. We calibrated the response of the radial modes to coherent excitation and implemented a laser-free method to determine the motional frequencies.
- I implemented a setup that allowed the same radio-frequency (RF) sources to produce bichromatic pulses with both the qubit laser and the electric field used for coherent driving. The setup was tested and built such that a stable phase relationship was maintained between the RF signals and between the two different arms of delivery.
- I was heavily involved in the implementation of a magnetic field shielding around our experimental system which led to a roughly 4-fold increase in the coherence times of the qubit transition. This allowed for significantly better results to be obtained when driving Rabi oscillations on sideband transitions.
- Before the results were obtained I was also involved in implementing a setup for single ion addressing (that had been developed and tested by Tommaso Faorlin) in our experimental system. The additional optics led to a reduction in the available laser power on the ion. I was therefore involved in extensively optimizing all parts of the qubit laser setup in order to obtain sufficient power to perform near-perfect sideband cooling and efficient population transfer on sideband transitions, which were both necessary requirements to improve the observation of the interference effects with a single phonon.
- After initial attempts to observe the interference effects for a single phonon were unsuccessful, I realized that the stability of the motional modes in our system was limiting the efficiency of bichromatic operations (addressing both modes simultaneously). I determined that noise in the RF signal used to generate the oscillating trapping field was the cause and switched to a new RF source that was significantly more stable.
- Robin and I carried out all of the data analysis, with simulations based on theoretical work by Alan Santos.
- Robin and I both developed individual schemes to produce the product state with a single phonon in each mode.

- I wrote the manuscript with input from Alan and Robin and discussion with all other authors.

### 1.1.2 Publication II

*Single-shot measurements of phonon number states using the Autler-Townes effect.* Marion Mallweger, Murilo Henrique de Oliveira, Robin Thomm, Harry Parke, Natalia Kuk, Gerard Higgins, Romain Bachelard, Celso Jorge Villas-Boas, Markus Hennrich. *Phys. Rev. Lett.*, **131**, 223603 (2023).

My contributions to this work are:

- I, along with Marion Mallweger, implemented and optimized the novel measurement technique described in the paper.
- I helped to obtain the initial results and contributed to the discussion of improvements and developments that were made to produce the final results in the paper.
- To avoid excessive AC Stark shifts when using strong coupling beams on the sideband transitions, Marion and I set up a method to perform AC Stark compensation during the detection scheme (in the end the results obtained without compensation were sufficiently good to be included in the publication, but the compensation scheme has been added to several other experiments).
- I contributed to the discussion in the writing of the manuscript.

### 1.1.3 Publication III

*Motional-state analysis of a trapped ion by ultranarrowband composite pulses.* Marion Mallweger, Milena Guevara-Bertsch, Boyan T. Torosov, Robin Thomm, Natalia Kuk, Harry Parke, Christian F. Roos, Gerard Higgins, Markus Hennrich, Nikolay V. Vitanov. *Phys. Rev. A*, **110**, 053103 (2024).

My contributions to this work are:

- I helped in the setup and implementation of the pulse sequences.
- I contributed to discussions of the results, experimental optimization and analysis.
- I contributed to the discussion in the writing of the manuscript.

### 1.1.4 Publication IV

*Observation of second- and higher-order electric quadrupole interactions with an atomic ion.* Gerard Higgins, Chi Zhang, Fabian Pokorny, Harry Parke, Erik Jansson, Shalina Salim, Markus Hennrich. *Phys. Rev. Research*, **3**, 032032 (2021).

My contributions to this work are:

- I, along with Erik Jansson and Shalina Salim, carried out the preparation, optimization and data acquisition for all of the measurements performed on the Rydberg  $56S_{1/2}$  and  $56P_{1/2}$  states, including making first use of a novel dressed-state spectroscopy technique proposed by Chi Zhang.
- I implemented the technique proposed by Gerard Higgins to measure the strength of the modulation sidebands using the Autler-Townes effect and performed all of the setup and measurements on the Rydberg  $46S_{1/2}$  states.
- I performed initial data analysis and re-measured the Rydberg resonance shifts several months after the initial measurements had been performed to verify the experimental results, allowing for an issue in the theoretical model to be identified and resolved.
- I contributed to the discussion of results and writing of the manuscript.

### 1.1.5 Publication V

*Micromotion minimization using Ramsey interferometry.* Gerard Higgins, Shalina Salim, Chi Zhang, Harry Parke, Fabian Pokorny, Markus Hennrich. *New J. Phys.* **23** 123028 (2021).

My contributions to this work are:

- I contributed to general improvements and maintenance of the experimental setup over the time that these results were obtained.
- I contributed to the discussion of results and writing of the manuscript.

# 2

## Theoretical background

---

Provided in this chapter are brief descriptions of the key theoretical components of the various experiments included in this thesis. Each section is intended to summarise the relevant concepts; exhaustive derivations are therefore omitted. Simplified derivations are however included throughout most of the chapter such that the key concepts are still clear and understandable without the need for external resources. The concepts covered in this chapter are: ion trapping basics, trapped ion motion, atom-light interactions and the response of a Rydberg ion to a trapping field.

### 2.1 Ion trapping

Confinement of charged particles can be achieved by various combinations of electric and magnetic fields. Although 3D confinement solely by static electric fields is prohibited by Earnshaw's theorem [56], a dynamically stable saddle point can be achieved using a radio-frequency (RF) oscillating electric field. Such confinement has been realised in various experimental configurations [57–59], the most typical of which is the linear Paul trap depicted in figure 2.1. Confinement in the plane perpendicular to the trap axis (from here on referred to as the radial direction or xy-plane) is achieved by an oscillating quadrupole field generated by RF voltages  $V = V_0 \cos(\Omega_{rf}t)$  on opposite pairs of electrodes. The radial quadrupole field extends along the length of the electrodes allowing dynamically-stable confinement along the entire axis of the trap. Confinement in the axial (or z-) direction is achieved by an additional static quadrupole field aligned parallel to the trap axis, which is produced by a DC voltage  $U_0$  on the electrodes labelled as endcaps in figure 2.1. A radial static quadrupole field or equivalently a DC offset  $V_f$  to the oscillating trapping field can also be used to break the symmetry of the confining potential in the radial plane. This allows for the motion in the x- and y-directions to be spectrally resolved. With such a configuration the quadrupole potential close

to the trap axis takes the form

$$\begin{aligned} \Phi(\mathbf{r}, t) &= \frac{x^2 - y^2}{2r_0^2} (V_0 \cos(\Omega_{rf}t) + V_f) \\ &+ \frac{\kappa}{2z_0^2} U_0 (2z^2 - x^2 - y^2), \quad x, y \ll r_0 \end{aligned} \quad (2.1)$$

where  $\kappa$  is a geometrical factor ( $\approx 0.042$  for our trap design),  $r_0$  is the distance between the radial electrodes and trap center and  $z_0$  is the distance between the two endcap electrodes. At this stage it is assumed that the polarizability of the charged particle confined by the trap has a negligible impact on the confining potential. This is typically a fair assumption for ions trapped in low-lying electronic states but is no longer valid when confining highly-polarizable molecules or Rydberg ions, the latter case is discussed in more detail in section 2.4.2.

For a particle with charge  $Q$  and mass  $m$  experiencing the potential given by Eq. 2.1, the equations of motion can be written as

$$m\ddot{x} = -Q \frac{d}{dx} \Phi(\mathbf{r}, t) = -2Qx(\alpha \cos(\Omega_{rf}t) + \gamma - \beta) \quad (2.2)$$

$$m\ddot{y} = -Q \frac{d}{dy} \Phi(\mathbf{r}, t) = 2Qy(\alpha \cos(\Omega_{rf}t) + \gamma + \beta) \quad (2.3)$$

$$m\ddot{z} = -Q \frac{d}{dz} \Phi(\mathbf{r}, t) = -4Qz\beta \quad (2.4)$$

where  $\alpha = V_0/2r_0^2$ ,  $\beta = \kappa U_0/2z_0^2$  and  $\gamma = V_f/2r_0^2$ . By making the substitution  $\tau = \Omega_{rf}t/2$  the above can be written canonically in the form of Mathieu equations

$$\frac{d^2x}{d\tau^2} + (a_x + 2q_x \cos(2\tau))x = 0. \quad (2.5)$$

$$\frac{d^2y}{d\tau^2} + (a_y + 2q_y \cos(2\tau))y = 0, \quad (2.6)$$

$$\frac{d^2z}{d\tau^2} + (a_x + a_y)z = 0. \quad (2.7)$$

The substitutions  $a$  and  $q$  are known as stability parameters and given by

$$a_x = \frac{8Q(\gamma - \beta)}{m\Omega_{rf}^2}, \quad a_y = -\frac{8Q(\gamma + \beta)}{m\Omega_{rf}^2} \quad \text{and} \quad q_x = -q_y = \frac{4\alpha Q}{m\Omega_{rf}^2}. \quad (2.8)$$

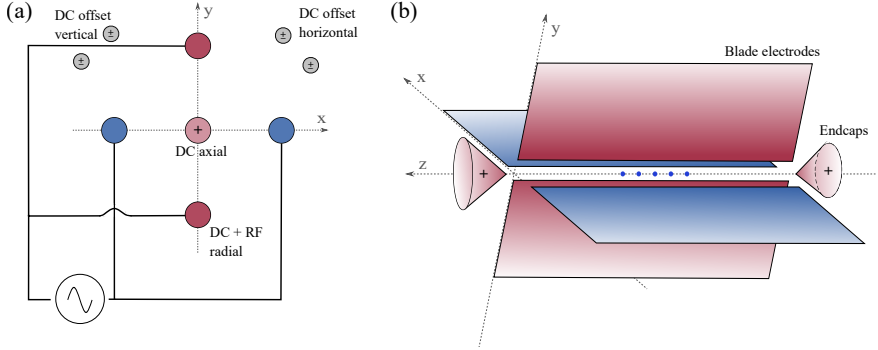


FIG. 2.1: Trap electrode geometry: (a) Schematic showing how the radiofrequency quadrupole trapping fields are generated. DC voltages are applied to sets of compensation electrodes (shown in grey) to make small adjustments to the ion’s position at the trap center, such that the electric field experienced by the ion is minimised. (b) Schematic of a typical “Innsbruck” design linear Paul trap with four radial electrodes spaced equidistant from one another in the  $x$ - $y$  plane and two endcap electrodes spaced apart in the  $z$ -direction.

Successful trapping of a charged particle, depending on its charge  $Q$  and mass  $m$ , is only achieved for certain values of  $a$  and  $q$ . Thus for a certain trap design the endcap and radial voltages as well as the oscillation frequency are tuned to provide stable confinement of particles of a certain charge-mass ratio [1]. It is therefore possible to configure ion traps to be species- and isotope-selective [60] and allows for the swift ejection of ions that become ionised beyond the stable charge-mass ratio [61].

For a trap operating with the quadrupole potential described in Eq. 2.1 the motion of a charged particle at its center occurs in two forms; secular motion is a harmonic oscillation of the particle at a frequency  $\omega_i$ , where  $i = \{x, y, z\}$ . Micromotion is a faster oscillation driven directly by the electric field at the frequency  $\Omega_{rf}$ . The extent of an ion’s micromotion is determined by the strength of the oscillating quadrupole field experienced at its average position, excess micromotion generally leads to unwanted effects in trapped ion experiments, one example would be the introduction of modulation sidebands in transition spectra [62]. In our experiment excess micromotion largely stems from a mismatch of the null positions of the DC and RF components of the quadrupole field, such that the ion’s average position is centered at a point in space where  $\langle \mathbf{E} \rangle \neq 0$ . Compensation is thus performed by applying DC voltages to additional sets of electrodes, which are depicted in figure 2.1. Tuning these voltages shifts the position of the static field null, allowing it to be overlapped with the null of the oscillating field and thereby

minimising the direct driving of ion motion. It should be noted, however, that some level of micromotion is inherent to a dynamically trapped ion as it oscillates about the trap centre.

The secular motional frequency is typically much smaller than  $\Omega_{rf}$  and characterises the harmonic pseudo-potential in which the trapped particle is bound. Secular motion arises due to a pondermotive force experienced by the ion as it is both pushed inwards and pulled outwards in a single direction during one full cycle of the electric field oscillation. As the electric field strength increases with distance from the trap centre the pondermotive force acts to confine the ion. The secular motion is therefore defined by the gradient of the electric field in the ion trap, a stronger applied field which necessarily covers the same volume and has a null at the trap centre will result in a larger electric field gradient and subsequently, faster secular motion. Close to the trap center the 3D pseudo-potential for this harmonic motion takes the form

$$U = \frac{m}{2}(\omega_x^2 x^2 + \omega_y^2 y^2 + \omega_z^2 z^2), \quad (2.9)$$

and trapping frequencies  $\omega_x$ ,  $\omega_y$  and  $\omega_z$  can be derived from Eqs. 2.5, 2.6 and 2.7 respectfully as

$$\omega_j = \frac{\Omega_{rf}}{2} \sqrt{\frac{q_j^2}{2} + a_j} \quad \text{and} \quad \omega_z = \sqrt{\frac{4Q\beta}{m}}, \quad (2.10)$$

where in this case  $j = \{x, y\}$ . Generally for linear Paul traps  $r_0 \ll z_0$  and  $a \approx 0$ , following this approximation we typically operate our trap with  $q \approx 0.3$  and  $\Omega_{rf} = 2\pi \times 18.4\text{MHz}$  which leads to trapping frequencies of  $\omega_{x,y} \sim 2\pi \times 1.7\text{MHz}$  and  $\omega_z \sim 2\pi \times 0.8\text{MHz}$ . The non-zero DC component of the quadrupole field which lifts the degeneracy of the x- and y-motional modes is set using a stable battery voltage of 1.5V, corresponding to a frequency splitting of  $\sim 70\text{kHz}$  between  $\omega_x$  and  $\omega_y$ .

## 2.2 Bounded motional states

### 2.2.1 Fock states

In this section we describe the possible quantum states of motion for a single trapped ion [22]. Considering a single direction, the motion of an ion experiencing the harmonic potential given by Eq. 2.9 is described by the Hamiltonian

$$\hat{H}_m = \hbar\omega_m(\hat{a}^\dagger\hat{a} + \frac{1}{2}), \quad (2.11)$$

where  $\omega_m$  describes the trapping frequency and  $\hat{a}^\dagger$  and  $\hat{a}$  are the creation and annihilation (or ladder) operators, whose product is the number operator

$$\hat{N} = \hat{a}^\dagger\hat{a}. \quad (2.12)$$

The eigenstates of  $\hat{N}$  are the number states  $\{|n\rangle\}$  (also known as Fock states) and are characterized by their definite particle number. These number states are connected via the ladder operators in the following manner

$$\hat{a}^\dagger|n\rangle = \sqrt{n+1}|n+1\rangle \quad (2.13)$$

$$\hat{a}|n\rangle = \sqrt{n}|n-1\rangle, \quad (2.14)$$

and can be formed by repeated application of  $\hat{a}^\dagger$  on the vacuum (or ground) state,

$$|n\rangle = \frac{1}{\sqrt{n!}} (\hat{a}^\dagger)^n |0\rangle. \quad (2.15)$$

We will see in the following section that the treatment of an ion's motion in the Fock basis is convenient to describe interactions with light and also in the simulation of other physical systems (such as atoms in cavities). In this description any motional state can be represented by a superposition of particular Fock states.

### 2.2.2 Thermal states

A trapped ion that has been Doppler cooled [63] exists in a thermal state, which can be described by an incoherent population of Fock states following a Boltzmann distribution. However, a thermal state is only meaningfully described by considering either an ensemble or - as in the case for a single ion - entanglement with a sufficiently large reservoir. The large number of photons scattered during Doppler cooling constitutes such a coupling, as a result the ion's motion is no longer accurately described by a pure state. Instead, the state of the system is described by a density matrix of the following form [22]

$$\rho_{th} = \frac{1}{\bar{n}+1} \sum_n \left( \frac{\bar{n}}{\bar{n}+1} \right)^n |n\rangle\langle n|, \quad (2.16)$$

where  $\bar{n}$  is the average phonon number for the distribution. The corresponding temperature of the system can be derived as

$$T = \frac{\hbar\omega_m}{k_b \ln \frac{\bar{n}+1}{\bar{n}}}. \quad (2.17)$$

### 2.2.3 Coherent states

Coherent (also referred to as Gaussian or Glauber) states can also be formed in a trapped ion system; they can be defined as displaced vacuum states (for which both  $N|0\rangle = 0$  and  $\hat{a}|0\rangle = 0$ ) and share the same minimum uncertainty in both particle number and phase. As a result they are *classical-like* in their properties and unchanged by the subtraction of a single quantum, which defines them as eigenstates of the annihilation operator,

$$\hat{a}|\alpha\rangle = \alpha|\alpha\rangle. \quad (2.18)$$

In the Fock basis the coherent state is defined as [22]

$$|\alpha\rangle = \sum_n \frac{\alpha^n}{\sqrt{n!}} e^{-\frac{|\alpha|^2}{2}} |n\rangle, \quad (2.19)$$

where  $|\alpha|^2 = \bar{n}$  if  $\bar{n}$  is the average number of phonons in a Poissonian distribution of number states. The properties of coherent states make them a valuable tool to study the boundary between classical and non-classical phenomena. In chapter 4 we generate both Fock and coherent states to study the effects of interference between two motional modes.

## 2.3 Atom-light interactions

### 2.3.1 Resonant coupling to a free atom

In this section the interaction of a coherent light field and a single atom will be briefly summarized, following the approach given in [64]. The atom is defined as a two-level system with ground state  $|g\rangle$  and excited state  $|e\rangle$  separated by  $\hbar\omega_a$  and the light field is characterized by a monochromatic plane wave with frequency  $\omega_l$ , amplitude  $E_0$  and phase  $\phi_l$ . The field can be decomposed into positive and negative frequency components as

$$\mathbf{E}(t) = \mathbf{E}_0 \cos(\omega_l t + \phi_l) \quad (2.20)$$

$$= \mathbf{E}_0^{(+)} e^{-i(\omega_l t + \phi_l)} + \mathbf{E}_0^{(-)} e^{i(\omega_l t + \phi_l)}. \quad (2.21)$$

The total Hamiltonian of the system is given by the sum of the atomic and interaction Hamiltonians; the latter of which is first considered as the response of the atom's electric dipole moment to the external field,

$$\hat{H} = \hat{H}_a + \hat{H}_d \quad (2.22)$$

$$= -\frac{1}{2}\hbar\omega_a\hat{\sigma}_z - \hat{\mathbf{d}} \cdot \mathbf{E}, \quad (2.23)$$

where  $\hat{\sigma}_z = |g\rangle\langle g| - |e\rangle\langle e|$  is the Pauli spin operator for the principal axis and  $\hat{\mathbf{d}}$  is the atomic dipole operator. Classically  $\hat{\mathbf{d}} = -e\hat{\mathbf{r}}$ , where  $\hat{\mathbf{r}}$  is then the electron position operator with respect to the atomic nucleus. In the above the dipole approximation, in which the spatial extent of the atom is negligible compared to the wavelength of the light field, has been assumed. Typically  $\omega_a$  will correspond to an optical transition, for which the wavelength is on the order of  $\sim 500\text{nm}$ . But even for higher energy photons the approximation remains valid, given that the size of the free atom is on the order of  $\sim 1\text{\AA}$ . In section 2.3.6 we consider an ion whose motion is bound by a potential of the form of Eq. 2.9, in this case the spatial extent of the ion is significantly larger and can no longer be completely neglected. For the isolated two-level system treated here the dipole operator can be considered in terms of the atomic eigenstates, for which the diagonal matrix elements will vanish to produce,

$$\hat{\mathbf{d}} = -e\{\langle e|\hat{\mathbf{r}}|g\rangle|e\rangle\langle g| + \langle g|\hat{\mathbf{r}}|e\rangle|g\rangle\langle e|\}. \quad (2.24)$$

By closing each side of the equation above with the identity operator  $\hat{I} = (|e\rangle\langle e| + |g\rangle\langle g|)$  and assuming that the off-diagonal matrix elements are real we obtain the result

$$\begin{aligned} \hat{\mathbf{d}} &= -e\langle g|\hat{\mathbf{r}}|e\rangle(\hat{\sigma}^- + \hat{\sigma}^+) \\ &= \hat{\mathbf{d}}^{(+)}(t) + \hat{\mathbf{d}}^{(-)}(t), \end{aligned} \quad (2.25)$$

where  $\hat{\sigma}^+ = |e\rangle\langle g|$  and  $\hat{\sigma}^- = |g\rangle\langle e|$  are the Pauli raising and lowering operators respectively. For clarity we maintain this convention for the use of Pauli operators over state projectors throughout this section. By representing the dipole operator in this way we highlight an implicit time dependence due to the free evolution of the atomic eigenstates (which would be considered by the expectation values of  $\hat{\sigma}^+$  and  $\hat{\sigma}^-$ ; the corresponding frequencies are  $+\omega_a$  and  $-\omega_a$ ). The resulting atom-field interaction is simplified by applying a rotating wave approximation (RWA) to remove all terms that oscillate far from the transition frequency  $\omega_a$ , which the

coherent field frequency  $\omega_l$  is assumed to be close to. Neglecting such terms leaves the interaction Hamiltonian as

$$\begin{aligned}\hat{H}_d &= -\hat{\mathbf{d}}^{(+)} \cdot \mathbf{E}^{(-)} - \hat{\mathbf{d}}^{(-)} \cdot \mathbf{E}^{(+)} \\ &= -e\langle g|\hat{\mathbf{r}} \cdot \boldsymbol{\epsilon}|e\rangle \left( E_0^{(-)} \hat{\sigma}^- e^{i(\omega_l t + \phi_l)} + E_0^{(+)} \hat{\sigma}^+ e^{-i(\omega_l t + \phi_l)} \right). \\ &= \frac{\hbar\Omega}{2} \left( \hat{\sigma}^- e^{i(\omega_l t + \phi_l)} + \hat{\sigma}^+ e^{-i(\omega_l t + \phi_l)} \right),\end{aligned}\tag{2.26}$$

where  $\boldsymbol{\epsilon}$  is the field's polarization vector and the parameter  $\Omega$ , which is known as the Rabi frequency, has been defined as

$$\Omega = \frac{-eE_0\langle g|\hat{\mathbf{r}} \cdot \boldsymbol{\epsilon}|e\rangle}{\hbar}.\tag{2.27}$$

Here the components of the electric field  $E_0^{(+)}$  and  $E_0^{(-)}$  are assumed to be real to provide the amplitude  $E_0 = 2E_0^{(+)}$ . The Rabi frequency, which defines the overall coupling strength of the interaction, is therefore determined by the field amplitude, polarization and the change in angular momentum for the specific transition, on which the value of the matrix element depends [65]. For trapped ion experiments it is common to define a quantization axis with a strong magnetic field (often parallel with the trap axis for simplicity), in this case the change in angular momentum for any transition between Zeeman manifolds can be calculated with the Clebsch-Gordon coefficients,  $g$ -factors and geometric dependence of the setup (i.e. the angle between the laser  $\mathbf{k}$ -vector and the magnetic field and the angle between a linear field polarization of the incoming laser and the magnetic field).

The perturbing interaction Hamiltonian includes a time-dependence that is absent from the free atomic Hamiltonian, which otherwise causes evolution according to the unitary transformation

$$\begin{aligned}\hat{U}_a &= e^{-i\hat{H}_a t/\hbar} \\ &= \begin{pmatrix} e^{-i\frac{\omega_a}{2}t} & 0 \\ 0 & e^{i\frac{\omega_a}{2}t} \end{pmatrix},\end{aligned}\tag{2.28}$$

The dynamics of the system are therefore most-easily obtained by transforming from the Schrödinger to the interaction picture in the following manner

$$\hat{H}_I = \hat{U}_a^\dagger \hat{H}_d \hat{U}_a\tag{2.29}$$

$$\begin{aligned}
&= \frac{\hbar\Omega}{2} \begin{pmatrix} e^{i\frac{\omega_a}{2}t} & 0 \\ 0 & e^{-i\frac{\omega_a}{2}t} \end{pmatrix} \begin{pmatrix} 0 & e^{-i(\omega_l t + \phi_l)} \\ e^{i(\omega_l t + \phi_l)} & 0 \end{pmatrix} \begin{pmatrix} e^{-i\frac{\omega_a}{2}t} & 0 \\ 0 & e^{i\frac{\omega_a}{2}t} \end{pmatrix} \\
&= \frac{\hbar\Omega}{2} (\hat{\sigma}^+ e^{-i(\Delta t + \phi_l)} + \hat{\sigma}^- e^{i(\Delta t + \phi_l)}), \tag{2.30}
\end{aligned}$$

where  $\Delta = \omega_l - \omega_a$  defines the detuning between the laser frequency and the atomic transition. When we are exactly on resonance ( $\Delta = 0$ ) the system evolves according to

$$\begin{aligned}
\hat{U}_I &= e^{-i\hat{H}_I t/\hbar} \\
&= \begin{pmatrix} \cos\left(\frac{\theta}{2}\right) & -ie^{-i\phi_l} \sin\left(\frac{\theta}{2}\right) \\ -ie^{i\phi_l} \sin\left(\frac{\theta}{2}\right) & \cos\left(\frac{\theta}{2}\right) \end{pmatrix}, \tag{2.31}
\end{aligned}$$

where  $\theta = \Omega t$  defines the polar angle for rotation on the Bloch sphere [64] between states  $|g\rangle$  and  $|e\rangle$  and the phase of the laser  $\phi_l$  defines the axis of rotation as  $\hat{\sigma}_{(n)} = \hat{\sigma}_x \cos(\phi_l) + \hat{\sigma}_y \sin(\phi_l)$ . For a fixed value of  $\Omega$  the continued action of  $U_I$  is to coherently exchange population between the ground and excited states of the isolated two-level system, this transfer is referred to as Rabi flopping. This can be a useful measure of both the coupling strength  $\Omega$  and decoherence in the system, which has not been considered in the derivations above, but can be observed as a dampening of the oscillations between the two states. In this case the system evolves in a non-unitary fashion until a steady-state of equivalent optical pumping between  $|g\rangle \leftrightarrow |e\rangle$  is obtained.

Rabi oscillations can still be observed for small values of  $\Delta$ , however in this case the non-zero detuning has an impact on the system's evolution. The dynamics of a near-resonant interaction are best obtained by solving the equation for time evolution in the interaction picture, for an initial state  $\psi(t)$  we have

$$i\hbar \frac{\partial}{\partial t} |\psi(t)\rangle = \hat{H}_I |\psi(t)\rangle. \tag{2.32}$$

A full derivation of the solutions to this equation can be found in [64] (in which it is initially assumed that  $E_g = 0$  and subsequently  $\hat{H}_a = \hbar\omega_a |e\rangle\langle e|$ , this is so that the calculation is simplified when moving into the atom's rotating frame). The key result from solving Eq. 2.32 is that coherent population transfer between the two states occurs at a new, generalized Rabi frequency which is given by

$$\tilde{\Omega} = \sqrt{|\Omega|^2 + \Delta^2}. \tag{2.33}$$

Thus, regardless of its sign, a non-zero detuning causes faster Rabi oscillations. If we assume at time  $t = 0$  that  $|\psi(0)\rangle = |g\rangle$  the solutions to Eq. 2.32 are simplified

further [64]; the resulting excited state population is given by

$$P_e = \frac{\Omega^2}{\tilde{\Omega}^2} \sin^2 \left( \frac{\tilde{\Omega}}{2} t \right). \quad (2.34)$$

The above expression shows that the non-zero detuning has an additional effect on the Rabi oscillations, as  $\Delta$  increases the amplitude of the oscillations decreases. Considered in terms of Bloch sphere rotation, these effects can be represented by an additional precession with magnitude  $\Delta t$  about the axis defined by  $\sigma_z$ . The additional precession combines with the rotation produced by the base coupling strength  $\Omega$  such that the overall axis of rotation is tilted off from the equator, as a result the state vector never fully reaches the excited state pole and traces a smaller circle on the surface of the Bloch sphere.

### 2.3.2 Off-resonant coupling

In real systems the validity of approximating a two-level system as being isolated from all other transitions will vary depending on a range of experimental parameters. Off-resonant driving may be an issue when Zeeman sub-levels are non-degenerate but closely spaced or when addressing sideband transitions. The two main consequences of this off-resonant coupling are unwanted population transfer and AC Stark shifts. Unwanted population transfer is quantified by Eq. 2.34. For significantly large detunings ( $|\Delta| \gg \Omega$ ) the maximum population transfer is then limited by the factor  $\Omega^2/\Delta^2$ . The AC Stark shift can be derived by first considering the atom-light system in a new coupled basis.

### 2.3.3 Dressed-states and the AC Stark effect

The dressed-state formalism is an alternate method to describe the interaction between a light field and a single-two level system (in this section we consider only classical fields, but the dressed-state formalism is equally applicable and commonly used when the coupling field is quantized). Again we follow the approach given in [64] and begin by taking the Hamiltonians  $\hat{H}_a$  and  $\hat{H}_d$  after the application of the rotating wave approximation, we then perform a transformation into the rotating frame of the laser at frequency  $\omega_l$  to remove all explicit time dependence. The full system Hamiltonian is then given by

$$\begin{aligned} \hat{H}' &= \hat{H}'_a + \hat{H}'_d \\ &= \frac{\hbar\Delta}{2} \hat{\sigma}_z + \frac{\hbar\Omega}{2} (\hat{\sigma}^- + \hat{\sigma}^+) \end{aligned} \quad (2.35)$$

$$= \frac{\hbar}{2} \begin{pmatrix} \Delta & \Omega \\ \Omega & -\Delta \end{pmatrix}. \quad (2.36)$$

In the new rotating frame the bare atomic eigenstates are separated by  $\hbar\Delta$ , with the sign of the detuning dictating their respective positions. However the presence of the coupling field means that these are no longer suitable eigenstates of the total system. Diagonalization of the above Hamiltonian produces the new eigenstates

$$|+\rangle = \sin(\theta)|g\rangle + \cos(\theta)|e\rangle \quad (2.37)$$

$$|-\rangle = \cos(\theta)|g\rangle - \sin(\theta)|e\rangle, \quad (2.38)$$

which are known as dressed states. The mixing angle  $\theta$  is given by

$$\tan(2\theta) = -\frac{\Omega}{\Delta}, \quad 0 \leq 2\theta < \pi. \quad (2.39)$$

Thus in this coupled picture the dressed states are a superposition of the original bare atomic eigenstates. On resonance ( $\Delta = 0$ ) there is an equal contribution from each of the bare states, whereas for large positive detunings the dressed states  $|+\rangle$  and  $|-\rangle$  approach  $|g\rangle$  and  $|e\rangle$  respectively (for large negative detunings, the reverse is true). The corresponding eigenvalues of  $\tilde{H}$  are found to be

$$\begin{aligned} E_{\pm} &= \pm \frac{\hbar}{2} \sqrt{\Omega^2 + \Delta^2} \\ &= \pm \frac{\hbar}{2} \tilde{\Omega}, \end{aligned} \quad (2.40)$$

where we have once again substituted for the generalized Rabi frequency. Rabi oscillations in the dressed-state picture are represented by a relative phase evolution between the two coupled eigenstates  $\{|\psi(t)\rangle = |+\rangle + e^{i\tilde{\Omega}t}|-\rangle\}$ , note here that the effects of a non-zero detuning obtained in section 2.3.1 are explained neatly by the presence of  $\Delta$  in both the eigenvalues and the weighting of bare state components in the eigenstates. A comparison between the dressed and bare state eigenenergies is given in figure 2.2 below.

The eigenvalues obtained above show that the dressed states are shifted from the bare atomic levels in any instance where the coupling field is present ( $\Omega > 0$ ). For a large detuning  $|\Delta| \gg \Omega$  we can perform a Taylor expansion of the expression for the generalized Rabi frequency in order to determine the shift of the ground state energy. Assuming a large negative detuning, figure 2.2 shows that  $|g\rangle$  and  $|-\rangle$  become comparable in energy. Experimentally this is achieved by red-shifting the

laser frequency below that of the bare atomic transition ( $\omega_l < \omega_a$ ); the resulting shift of the ground state energy level due to the far off-resonant field is given by the difference between  $E_-$  and  $E_g$ , as follows

$$\begin{aligned} \delta_g &= E_- - E_g \\ &= -\frac{\hbar\tilde{\Omega}}{2} + \frac{\hbar|\Delta|}{2} \\ &\approx -\frac{\hbar|\Delta|}{2} \left(1 + \frac{\Omega^2}{2\Delta^2}\right) + \frac{\hbar|\Delta|}{2} = -\frac{\hbar\Omega^2}{4|\Delta|} = \frac{\hbar\Omega^2}{4\Delta}. \end{aligned} \quad (2.41)$$

The additional energy shift is dependent on the strength and detuning of the laser from the bare atomic resonance. This shift is known as the AC Stark effect. With  $\Delta < 0$  we see the ground state is shifted down in energy, the equivalent shift of the excited state, which can be calculated similarly as the difference between  $E_+$  and  $E_e$ , is in the opposite direction. The result is an increase (blue shift) of the transition frequency for  $|g\rangle \leftrightarrow |e\rangle$  by

$$\delta_{eg} = \frac{\hbar\Omega^2}{2\Delta}. \quad (2.42)$$

The form of the AC Stark shift indicates that a transition can also be red-shifted when the laser is instead detuned positively from the resonance, in this case the ground state is shifted up and the excited state down, reducing the overall

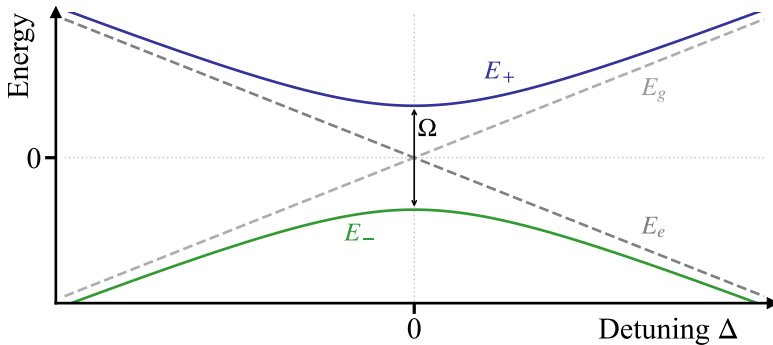


FIG. 2.2: The bare energy levels of an isolated two-level system (gray) become dressed states (blue and green) when a coupling field of strength  $\Omega$  is present. For large positive or negative detunings the dressed states reduce approximately to the original uncoupled energy levels. When the coupling field is tuned close to the resonance of the atomic transition an avoided crossing is observed between the two eigenstates.

transition frequency. In either case the shift is proportional to the intensity of the off-resonant light field in contrast to the resonant coupling (defined by Rabi oscillations) which is proportional to the amplitude. The AC Stark shift (also known as a light shift) has various applications in an ion trap system. It is an essential component of certain laser cooling techniques, such as polarisation gradient cooling [66, 67] and can be a valuable tool to improve the addressing of single qubit operations [68], align non-resonant laser beams, obtain estimates of laser power at the ion position [69] and compensate for unwanted resonance shifts [69].

### 2.3.4 Autler-Townes effect

The Autler-Townes effect [70] is a resonant phenomenon that occurs in three-level systems and is effectively described using the dressed-state formalism. For the works presented in this thesis, the Autler-Townes effect is employed for motional state detection in chapter 5 and for Rydberg state spectroscopy in chapter 7. We label the three states involved  $|1\rangle$ ,  $|2\rangle$  and  $|3\rangle$  and assume only that they are non-degenerate and that levels  $|2\rangle$  and  $|3\rangle$  are initially unpopulated. The Autler-Townes effect occurs when a weak probe is applied to the transition  $|1\rangle \leftrightarrow |2\rangle$  at the same time as the transition  $|2\rangle \leftrightarrow |3\rangle$  is strongly coupled by an additional field. The effect of the strong coupling field, when applied on or close to resonance, can be described by the dressed-state formalism; the result is a splitting of the  $|1\rangle \leftrightarrow |2\rangle$  resonance into two separate absorption peaks, known as an Autler-Townes doublet. The splitting between the two peaks is equivalent to the energy separation between the dressed states ( $\hbar\tilde{\Omega}_c$ ). Whilst the original resonance for the transition  $|1\rangle \rightarrow |2\rangle$  is completely suppressed, for  $\Delta_p = -\hbar\tilde{\Omega}_c/2$  the transition  $|1\rangle \rightarrow |- \rangle$  is driven, similarly for  $\Delta_p = +\hbar\tilde{\Omega}_c/2$  the transition  $|1\rangle \rightarrow |+\rangle$  is probed. For the Autler-Townes effect to be observed we require

$$\tilde{\Omega}_p, \Gamma_2, \Gamma_3 \ll \tilde{\Omega}_c, \quad (2.43)$$

where  $\tilde{\Omega}_p$ ,  $\tilde{\Omega}_c$  are the generalized Rabi frequencies of the probe and coupling beams respectively and  $\Gamma_2$  and  $\Gamma_3$  are the decay rates of the strongly coupled states. The Autler-Townes splitting can be employed as a useful spectroscopic tool in two ways: if the quantity  $\tilde{\Omega}_c$  is unknown but may provide some knowledge of a system's properties it can be efficiently determined by observing the position of either of the two doublet peaks. If the resonance frequency of the transition  $|2\rangle \leftrightarrow |3\rangle$  is not known then the coupling laser detuning can be scanned whilst observing the effect on the weakly probed transition (which is held at a fixed frequency  $\Delta_p = 0$ ). When the coupling beam becomes resonant, the excitation of the probed transition will drop due to the doublet formation.

### 2.3.5 Quadrupole transitions

We note here that simply by changing the form of the Rabi frequency the Hamiltonian given by Eq. 2.26 which was derived assuming a simple dipole coupling, is equally valid for both quadrupole and Raman transitions [22]. For the works included in this thesis the former is of particular importance, as we employ a quadrupole transition to define optical qubits in trapped Strontium ions. The quadrupole interaction is a second-order effect with respect to the spatial dependence of the electric field, which was previously neglected. Thus we must first redefine the monochromatic plane wave as

$$\mathbf{E}(t) = \mathbf{E}_0 \cos(\mathbf{k}_l \cdot \hat{\mathbf{r}} - \omega_l t), \quad (2.44)$$

where  $\mathbf{k}_l$  is the wavevector and  $\hat{\mathbf{r}}$  is the position operator, we have assumed a phase offset  $\phi_l = 0$  for simplicity. The Rabi frequency to describe the quadrupole transition then becomes

$$\Omega_q = \frac{-eE_0 \langle g | (\hat{\mathbf{r}} \cdot \boldsymbol{\epsilon}) (\mathbf{k}_l \cdot \hat{\mathbf{r}}) | e \rangle}{2\hbar}. \quad (2.45)$$

As before, the geometrical dependence of the transition matrix element plays a key role in determining which transitions are driven by an incoming laser beam. An expansion of Eq. 2.45 which offers more detail into this geometric dependence is available in [71].

### 2.3.6 Ion-phonon coupling for a trapped ion

In this section the atom-field interaction will be considered in terms of a single trapped ion and a coherent laser field. Spatial-dependence of both the field and the ion's bound motion are included in the derivations. No assumption is made on the form of the two-level system but it is useful to consider a quadrupole transition, as some of the results obtained later rely on a sufficiently narrow transition linewidth to be experimentally observable. The following derivation follows closely that provided by [71]. We can describe the full Hamiltonian of the system with three terms, describing the atom's internal electronic state, its quantized motional state and the interaction with the laser field as follows

$$\hat{H}_e = -\frac{1}{2} \hbar \omega_{eg} \hat{\sigma}_z, \quad (2.46)$$

$$\hat{H}_m = \hbar \omega_j (\hat{a}_j^\dagger \hat{a}_j + \frac{1}{2}), \quad (2.47)$$

$$\hat{H}_{int} = \frac{1}{2} \hbar \Omega (\hat{\sigma}^+ + \hat{\sigma}^-) (e^{i(\mathbf{k}_l \mathbf{r} - \omega_l t + \phi_l)} + e^{-i(\mathbf{k}_l \mathbf{r} - \omega_l t + \phi_l)}), \quad (2.48)$$

where  $\omega_{eg}$  is the characteristic frequency of the atomic transition,  $\omega_j$  is the motional frequency corresponding to the mode  $j = x, y, x$ . The Hamiltonian is valid under the assumption that the laser is resonant with only a single transition. If we consider only one direction, such that  $\mathbf{r}$  overlaps exactly with the oscillatory motion of the ion for the mode  $j$  the following substitution can be made

$$r = \sqrt{\frac{\hbar}{2m\omega_j}}(\hat{a}_j^\dagger + \hat{a}_j). \quad (2.49)$$

Since we are now considering the interaction Hamiltonian in terms of creation/annihilation operators for the ion's motion it is useful to introduce another simplification by defining the Lamb-Dicke parameter  $\eta$  as

$$\eta = k_l \cos \theta \sqrt{\frac{\hbar}{2m\omega_j}}, \quad (2.50)$$

where  $\theta$  is the angle between  $k_l$  and the ion's oscillatory motion. From here on we refer only to the addressed mode  $j$  and drop the relevant subscript notation for clarity. If we further assume that  $\theta = 0$  the interaction Hamiltonian is then given by

$$\hat{H}_{int} = \frac{1}{2}\hbar\Omega(\hat{\sigma}^+ + \hat{\sigma}^-) \left( e^{i(\eta(\hat{a}^\dagger + \hat{a}) - \omega_l t + \phi_l)} + e^{-i(\eta(\hat{a}^\dagger + \hat{a}) - \omega_l t + \phi_l)} \right). \quad (2.51)$$

At this stage it is useful to convert from the Schrödinger to the interaction picture by performing the transformation  $\hat{H}_I = \hat{U}^\dagger \hat{H}_{int} \hat{U}$  with  $\hat{U} = e^{i(\hat{H}_e + \hat{H}_m)t/\hbar}$ . The rotating wave approximation is applied so that any terms which would lead to oscillations much faster than  $\omega_{eg}$  are neglected and we are left with a Hamiltonian of the form

$$\hat{H}_I = \frac{1}{2}\hbar\Omega(\hat{\sigma}^+ e^{i(\phi_l - \Delta t)} e^{[i\eta(\hat{a}^\dagger e^{i\omega t} + \hat{a} e^{-i\omega t})]} + h.c.), \quad (2.52)$$

where  $\Delta = +\omega_l - \omega_{eg}$  is the detuning of the laser and  $h.c.$  is the hermitian conjugate. For an ion in the ground state  $|g\rangle$  and with phonon occupation number  $|n\rangle$  the above Hamiltonian indicates coupling from  $|g, n\rangle$  to all possible states  $|e, n'\rangle$  (including  $n' = n$ ) [71]. Pairwise coupling between two specific states of the motional manifold is achieved by tuning the laser close to a specific resonance and ensuring off-resonant coupling to other levels is small (i.e.  $\Omega \ll \omega$ ). Coupling between the light field and the ion's internal motional state arises due to the recoil energy imparted to or removed from the ion during absorption and emission processes. Within the ion's rest frame, as it oscillates in the direction of the incoming light field, it sees a frequency-modulated wave with sidebands at  $\omega_l \pm \beta\omega$  where  $\beta$

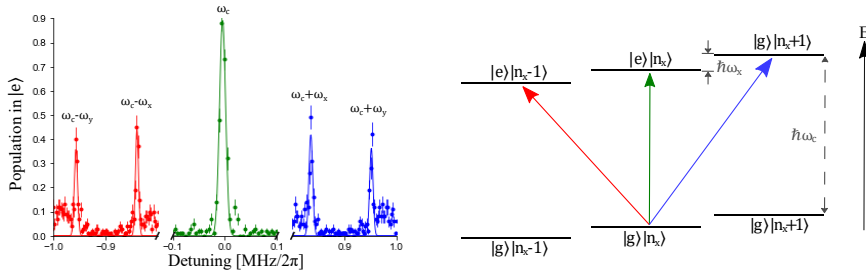


FIG. 2.3: Non-degenerate motional sideband transitions for a single trapped ion. Frequency spacings between the carrier  $\omega_c$  and red(blue) sideband transitions are shown for typical trap settings. The simplified “ladder” scheme shown on the right depicts how the motional mode population is altered for each of the red, blue and carrier transitions.

can take the value of any positive integer.

When a photon is absorbed or emitted at these sideband frequencies the ion recoils in order to conserve momentum in the system, this change in kinetic energy is equivalent to the loss or gain of some integer multiple of motional quanta. If the motional quantum number is reduced during the process the transition is referred to as a red sideband, if the motional quantum number is increased the transition is referred to as a blue sideband and if the motional quantum number remains unchanged the transition is referred to as the carrier, the various transitions are depicted between the ground and excited states of a two-level system in figure 2.3.

### 2.3.7 Lamb-Dicke regime

For many purposes in trapped ion experiments, such as resolved sideband cooling, it is necessary to work with a very weak coupling between the ion’s internal electronic and motional states. Such a coupling requires the recoil energy of the absorption/emission process to be small compared to the energy spacing between excitations of the motional mode. In this case transitions that change the motional quantum number by more than  $\pm 1$  are strongly suppressed. Resolved sideband cooling also requires that spontaneous emission overwhelmingly occurs via the carrier transition as opposed to the first red or blue sidebands. These conditions can be quantified by the following expression,

$$\eta^2(2n + 1) \ll 1. \quad (2.53)$$

If the condition above is satisfied the ion-laser system is said to be in the Lamb-Dicke regime; the spatial extent of the ion’s motion is much smaller than the wavelength of the incoming light field and transitions that change the phonon

number beyond  $\pm 1$  are only weakly accessible. It is worth noting that this refers to the entire system of the ion and the laser field since  $\eta$  is dependent on the wavelength of the light. The criterion is therefore more easily satisfied for some transitions than for others since a higher wavelength transition can reach the Lamb-Dicke regime at higher temperatures (larger  $n_j$ ) and does not require Doppler cooling to the same extent. In the Lamb-Dicke regime Eq. 2.52 can be greatly simplified by performing a Taylor expansion of the second exponential term,

$$e^{[i\eta(\hat{a}^\dagger e^{i\omega t} + \hat{a}e^{-i\omega t})]} \approx 1 + i\eta(\hat{a}^\dagger e^{i\omega t} + \hat{a}e^{-i\omega t}) + \mathcal{O}(\eta^2). \quad (2.54)$$

The final interaction Hamiltonian can be further simplified by inputting specific values of  $\Delta$  corresponding to the available transitions and neglecting any off-resonant terms. For the case where  $\Delta = 0$  the laser drives the carrier transition  $|g, n\rangle \leftrightarrow |e, n\rangle$  as per the interaction Hamiltonian

$$\hat{H}_{I_{carrier}} = \frac{1}{2}\hbar\Omega_{n \rightarrow n}(\hat{\sigma}^+ e^{i\phi_l} + \hat{\sigma}^- e^{-i\phi_l}), \quad (2.55)$$

where  $\Omega_{n \rightarrow n}$  is the phonon-number dependant coupling strength

$$\Omega_{n \rightarrow n} = (1 - \eta^2 n)\Omega_0. \quad (2.56)$$

In the above expression  $\Omega_0$  is the coupling strength of the  $(n = 0) \leftrightarrow (n = 0)$  transition (which is equivalent to the general Rabi frequency denoted simply as  $\Omega$  in previous equations). For the case where  $\Delta = -\omega$  the laser drives the red sideband transition  $|g, n\rangle \leftrightarrow |e, n - 1\rangle$  as per the interaction Hamiltonian

$$\hat{H}_{I_{red}} = \frac{1}{2}i\hbar\Omega_{n \rightarrow n-1}(\hat{\sigma}^+ \hat{a} e^{i\phi_l} - \hat{\sigma}^- \hat{a}^\dagger e^{-i\phi_l}) \quad (2.57)$$

with coupling strength

$$\Omega_{n \rightarrow n-1} = \eta\sqrt{n}\Omega_0. \quad (2.58)$$

For the case when  $\Delta = +\omega$  the laser drives the blue sideband transition  $|g, n\rangle \leftrightarrow |e, n + 1\rangle$  as per the interaction Hamiltonian

$$\hat{H}_{I_{blue}} = \frac{1}{2}i\hbar\Omega_{n \rightarrow n+1}(\hat{\sigma}^+ \hat{a}^\dagger e^{i\phi_l} - \hat{\sigma}^- \hat{a} e^{-i\phi_l}) \quad (2.59)$$

with coupling strength

$$\Omega_{n \rightarrow n+1} = \eta\sqrt{n+1}\Omega_0. \quad (2.60)$$

From the above it is clear that the carrier transition is much more strongly driven than either the red or blue sidebands when  $n$  is low, this is shown in the spectrum

plotted in figure 2.3. Whilst the Lamb-Dicke criterion is satisfied it is also possible to determine the temperature of the ion by performing Rabi oscillations [71], due to the dependence on  $n$  in Eqs. 2.56, 2.58 and 2.60.

### 2.3.8 Jaynes-Cummings interactions

The interaction Hamiltonian of Eq. 2.57 is also known as the Jaynes-Cummings Hamiltonian [72] and is commonly applied in cavity quantum electrodynamics (cavity QED) systems to describe the interaction between a single atom and a single cavity mode (a comprehensive review of the Jaynes-Cummings model and its various applications is available in [73]). In this case the photon, which in the above equations would be represented by the characteristic frequency  $\omega$  of the motional mode, must be close in energy to the separation  $\hbar\omega_{eg}$  such that energy is readily exchanged between the atom and cavity with a strength that depends on the overall coupling between them. For the case of a trapped ion, typically  $\omega_{eg} \gg \omega$  and interaction between the ion's motional and electronic states is negligible without the mediation of the additional light field. Nevertheless the laser-addressed trapped ion, when tuned to a regime given by Eq. 2.57, can provide an effective simulation of cavity QED. In chapter 4, a two-mode Jaynes-Cummings Hamiltonian is employed to produce novel motional states and simulate interference effects for an atom interacting with two cavity modes simultaneously.

### 2.3.9 Bichromatic fields

The atom-light interactions described by the Jaynes-Cummings Hamiltonian can also be neatly extended to include two interfering light fields interacting with a single atom. Bichromatic fields are a key component of one of the most widely-adopted trapped ion entanglement schemes, the Mølmer-Sorensen gate [21]. In this case the two tones of the bichromatic field are set either side of a carrier transition, with an equal but opposite detuning applied from the red and blue sideband transition frequencies respectively. For the works considered in this thesis the interest is in a bichromatic field where the two tones are set to the red (or blue) sideband transition frequencies of two separate motional modes simultaneously. With this the two-mode Hamiltonian can be derived by a summation of 2.57 (2.59) for two modes  $\{x, y\}$ . In the case of two red sidebands with equal coupling frequencies  $\Omega_x = \Omega_y = \Omega$  this gives the total interaction Hamiltonian

$$\hat{H}_{x,y} = \frac{1}{2}i\hbar\Omega \left( \hat{\sigma}^+ (\hat{a}_x e^{i\phi_x} + \hat{a}_y e^{i\phi_y}) - \hat{\sigma}^- (\hat{a}_x^\dagger e^{-i\phi_x} + \hat{a}_y^\dagger e^{-i\phi_y}) \right). \quad (2.61)$$

## 2.4 Trapped Rydberg ions

### 2.4.1 Rydberg ion properties

In this section a summary of the properties of Rydberg atoms will be provided. Rydberg atoms are formed by the excitation of a single valence electron to a high-lying orbital such that the principal quantum number  $n \gg 1$ . In this highly-excited state an atom's properties change dramatically due to their immense size; an atom in a Rydberg state of  $n = 50$  can be as large as 500nm in diameter [74]. The orbital radius of the highly-excited electron  $\langle r \rangle$  scales with the principal quantum number ( $n$ ) as  $n^2$  and the spacing between energy levels scales as  $n^{-3}$ . From here it is possible to derive scaling relations for several other Rydberg state properties, the most relevant for the works in this thesis are given below in table 2.1, a full list more relevant to general Rydberg atom and ion trapping experiments is given in table 1.1 of [74].

Property	Scaling
Natural lifetime $\tau_{nat}$	$n^3$
Electric dipole moment $d$	$n^2$
Electric quadrupole moment $\Theta$	$n^4$
Electric dipole polarisability $\alpha$	$n^7$
Electric quadrupole polarisability $\Sigma$	$n^{11}$
Dipole-dipole interaction strength $V_{dd}$	$n^4$
Van der Waals interaction strength $V_i$	$n^{11}$

Table 2.1: The scaling of several key Rydberg ion properties with respect to the principle quantum number  $n$ . Of particular note for this thesis are the electric dipole and quadrupole polarisabilities; the extreme scaling of such properties means that high-lying Rydberg states can be extremely sensitive to external electric fields and therefore valuable for metrology.

Rydberg state lifetimes are typically much longer than those of low-lying excited states due to the minimal overlap of wavefunctions between the outermost electron and those closer to the nucleus. The  $n^3$  scaling listed above is true in systems where the Rydberg state predominantly decays to low-lying states via the emission of short wavelength photons in the UV range. Such decay is dominant when coupling to the environment primarily occurs through vacuum modes, given the higher mode density at shorter wavelengths (scales as  $\omega^3$ ). In our system the trap is held at room temperature and decay from the Rydberg state is primarily mediated by black-body radiation (mode density scales as  $\omega^2$ ) [75]. In the latter

case decay predominantly occurs via long wavelength transitions to other Rydberg states, reducing the natural lifetime so that it scales as  $n^2$ . In our system this corresponds to Rydberg state lifetimes in the range of  $5 - 50\mu s$  for different angular momentum states at  $n \sim 50$ . Long lifetimes and strong dipole-dipole interactions are two of the major drawing points for the use of Rydberg atoms in quantum computing. In neutral atom systems, although state-of-the-art gate speeds are still far from the limit set by Rydberg state decay, high-fidelity two qubit gates on the  $\mu s$  time scale have been achieved [76–78].

In the case of Rydberg ions the primary form of interaction (assuming a lack of external fields or dressing) is a weak van der Waals coupling. Although this property scales favourably with the principle quantum number the overall strength of the coupling also depends on an effective core charge  $Z$  which is felt by the outermost electron. In the case of Rydberg ions the van der Waals coefficient scales unfavourably as  $Z^{-6}$ . Compared to two neutral Rydberg atoms, the interaction strength is therefore 64 times weaker and ultimately unsuitable for use in efficient gate schemes. To combat this issue gate schemes involving microwave dressing to induce strong dipole-dipole interactions were proposed [44, 75] and have since been implemented experimentally [50].

### 2.4.2 Dipole interaction with electric fields

In section 2.3.3 we derived the AC Stark effect, a consequence of off-resonant atom-light interaction. In this section we derive general expressions for Stark effects, which occur as a result of an atom’s interaction with any external electric field. The atom’s response is dictated by its charge distribution and in this case can be well approximated using perturbation theory. Again we take the position operator  $\hat{r}$  and the charge of a single electron  $e$  to obtain the transition dipole moment between an initial state  $|i\rangle$  and final state  $|f\rangle$ ,

$$\hat{d} = -e\langle i|\hat{r}|f\rangle. \quad (2.62)$$

If we now assume that the atom is placed into a uniform electric field with strength  $\varepsilon$  oriented along the z-axis and that any effects on the atomic energy levels due to fine structure splitting are negligible compared to the effects caused by the electric field, we can define an interaction Hamiltonian

$$\hat{H}_{Stark} = \hat{d}\varepsilon = -e\varepsilon\hat{z}, \quad (2.63)$$

where  $\hat{z}$  is a 1D position operator. We can then describe the first order energy shift caused by  $\hat{H}_{Stark}$  using non-degenerate perturbation theory as

$$E_{nlm}^{(1)} = e\varepsilon \langle \phi_{nlm} | \hat{z} | \phi_{nlm} \rangle, \quad (2.64)$$

where  $|\phi_{nlm}\rangle$  is the electronic wave function defined by quantum numbers  $n, l, m$ . For a uniform field the parity of  $\hat{z}$  is always odd, thus for any wavefunction with a definite parity, regardless of the values of  $n, l$  and  $m$  the element  $\langle \phi_{nlm} | \hat{z} | \phi_{nlm} \rangle$  is the integral of an odd function over all space along the z-axis and must be equal to zero. Any atom whose energy levels are non-degenerate with respect to the value of  $l$  will necessarily have a definite parity and will not experience the first order Stark effect. In the case of excited states of hydrogen the mixing of degenerate orbital angular momentum states allows the above integral to be non-zero, a permanent dipole moment is exhibited and the first order shift lifts the degeneracy in  $l$  [79].

For atoms without permanent dipole moments the dominant response to an electric field is produced by induced dipole moments. The energy shift in this case can be derived from second-order perturbation theory as

$$E_{nlm}^{(2)} = e^2 \varepsilon^2 \sum_{n', l', m'} \frac{|\langle \phi_{n'l'm'} | \hat{z} | \phi_{nlm} \rangle|^2}{|E_{n,l} - E_{n',l'}|}, \quad (2.65)$$

where the quantum numbers  $n', l'$  and  $m'$  are used to denote the neighbouring energy levels. One can see that the response given in the expression above depends on  $\varepsilon^2$  and is therefore labelled the quadratic Stark effect. Since the second-order shift arises from the interaction between the atom's induced dipole moment and the external electric field, we can relate it to the classic expression for an energy shift due to atomic polarizability  $\alpha$ ,

$$E_{nlm}^{(2)} \equiv \Delta E = -\frac{1}{2} \alpha \varepsilon^2. \quad (2.66)$$

By comparing equations 2.65 and 2.66 we obtain the following expression for the atomic dipole polarizability

$$\alpha = 2 \sum_{n', l', m'} \frac{|\langle \phi_{n'l'm'} | \hat{z} | \phi_{nlm} \rangle|^2}{|E_{n',l'} - E_{n,l}|}. \quad (2.67)$$

For Rydberg states  $\langle \phi_{n'l'm'} | \hat{z} | \phi_{nlm} \rangle$  scales with the size of the atom as  $n^2$ , thus the numerator in equation 2.67 scales as  $n^4$ . Taking into account that the energy difference between neighbouring Rydberg states scales as  $n^{-3}$ , we arrive at the extreme scaling of  $n^7$  for the electric dipole polarisability. Even with relatively low principal quantum numbers ( $n \sim 30$ ) the Rydberg atom can have a polarizability that is several orders of magnitude larger than for atoms in low-lying states. Stark effects due to the interaction between a trapped ion and a confining electric field are typically neglected due to the relatively weak response for low-lying states; this

is no longer true in the case of precise atomic clock experiments [80] as state-of-the-art frequency uncertainties are well below the limit of typical dipole-induced Stark shifts (but not quadrupole or beyond). For trapped Rydberg ions however, the significantly larger polarizabilities can lead to severe Stark shifts. Such a property can be both a valuable asset in experiments which benefit from an enhanced sensitivity to electric fields, or a severe hindrance in experiments which require exceptional isolation from all possible sources of external disturbance.

### 2.4.3 Higher-order interaction with electric fields

Permanent and induced dipole moments are sufficient to describe the idealised response of an atom to an external electric field; a more precise description must also include higher order responses of the complex configuration of multipoles that govern the atom's electrical properties [79]. After dipole terms the most significant response can typically be attributed to the atom's quadrupole moment (whether it be permanent or induced) which couples to the electric field gradient as opposed to the field strength. This is especially important to consider for the trapping of charged particles, in which confinement is almost exclusively provided by quadrupolar fields. Exceptions to this include octupolar trap designs [81] and the use of optical dipole forces to provide confinement [82, 83]. In a similar manner to the Stark shifts described above, the interaction of quadrupole moments with an external electric field gradient will alter the atomic energy spectrum. For our system of trapped Rydberg ions the quadrupole contributions cannot be dismissed due to the exceptionally large moments and polarizabilities that are experimentally achievable. Following a similar perturbative approach as for the dipole response shown above, scaling relations of  $n^4$  and  $n^{11}$  can be derived for the electric quadrupole moment and electric quadrupole polarisability respectively. So far the electric quadrupole moment of a single ion has been measured in trapped ion experiments with low-lying states [84] and with Rydberg ions [55] and has been shown to have a significant impact on the energy spectrum of the latter. In chapter 7 of this work an experiment is performed in which both the dipole response and interaction with the quadrupole moment are negligibly small, the result is an observation of the response of a single atom to an external electric field due to its quadrupole polarizability.

### 2.4.4 Rydberg state trapping potentials

The interaction between a Rydberg ion and the trapping electric field produces non-negligible changes in the trapping potential. As such there are several additional effects that have to be considered when an ion is excited to a Rydberg state.

These can be split into two cases, depending on whether the ion sees the trapping field due to its motion (the motional wavepacket for a trapped ion may overlap with regions of non-zero electric field strength, even if the field is equal to zero at the ion's average position) or due to imperfect micromotion compensation (which means a non-zero electric field strength at the ion's average position regardless of the extent of its motional wavepacket).

To determine the effects on the trapping potential we first re-write equation 2.1 in terms of time-dependent and static electric field gradients, labelled  $A$  and  $B$  respectively,

$$\Phi = A \cos(\Omega_{rft}) (x^2 - y^2) - B [(1 + \epsilon)x^2 + (1 - \epsilon)y^2 - 2z^2], \quad (2.68)$$

where  $\epsilon$  is used here to represent the lifted degeneracy between the two radial modes. The trapping field is given by

$$\boldsymbol{\varepsilon} = -\nabla\Phi. \quad (2.69)$$

To calculate the time-averaged electric field strength we first make use of the assumption that  $A^2 \gg B^2$  (which is valid for the typical operation of a linear Paul trap), the result is

$$\langle \boldsymbol{\varepsilon}^2 \rangle = 2A^2 (x^2 + y^2). \quad (2.70)$$

The energy shift induced as a result of the Rydberg ion's polarizability then takes the form of an additional harmonic trapping potential

$$\Delta U = -\frac{1}{2}\alpha\langle \boldsymbol{\varepsilon}^2 \rangle \approx -\alpha A^2 (x^2 + y^2), \quad (2.71)$$

which is added to the original potential described by equation 2.9 to give altered radial trapping frequencies

$$\omega'_i \approx \sqrt{\omega_i^2 - \frac{2\alpha A^2}{M}}, \quad (2.72)$$

where  $M$  is the ion mass and  $i = \{x, y\}$  denotes the radial mode. The effects are predominantly confined to the radial plane as the oscillating electric field ideally has no component in the axial direction; in practice small imperfections on the electrode surfaces and alignment will result in an unavoidable axial component that drives micromotion along the trap axis, but this is typically small enough to be neglected when the ions are roughly equidistant from the endcap electrodes [62].

In the case that the ion's equilibrium position is at the overlapping nulls of the

static and oscillating electric fields (i.e. perfectly micromotion compensated) the change in the trapping potential when exciting to a Rydberg state will depend on the number of phonons in each of the radial modes. The consequence is a shift in the resonance position of a transition between a low-lying state  $|l\rangle$  and a Rydberg state  $|r\rangle$  that is equal to

$$\Delta E_{l \rightarrow r} = n_x \hbar(\omega'_x - \omega_x) + n_y \hbar(\omega'_y - \omega_y). \quad (2.73)$$

Phonon-number-dependent resonance shifts pose an issue for the use of Rydberg states in entangling operations [44], particularly in longer ion crystals where cooling multiple motional modes to their respective ground states becomes cumbersome. Certain techniques, such as EIT cooling [85], have been shown to enable simultaneous motional ground state preparation over a wide frequency range but also suffer unwanted heating in orthogonal modes not addressed by the cooling beam [86]. This issue could also be resolved by removing the requirement for near-perfect ground state cooling in a longer ion crystal, one such method is to prepare Rydberg states with vanishing polarizabilities which are no longer sensitive to the trapping fields [87]. The main drawback of this solution is that Rydberg states with vanishing polarizabilities require unequal superpositions of  $nS$  and  $nP$  states (due to the unequal magnitude of the polarizabilities which are opposite in sign). Such superpositions are not maximally dressed by a microwave field and will therefore suffer smaller dipole-dipole interactions when employed to entangle qubits. In order to achieve stronger interactions, and consequently faster gate times with vanishing polarizability states, higher Rydberg states need to be realized [61].

In the case that micromotion is not well compensated and the ion's equilibrium position lies between the spatially-separated nulls of the static and oscillating trapping fields the effects of the Rydberg state polarizability are more severe. Such a situation typically arises when the null of the static quadrupole field is displaced from the trap centre; as with the axial micromotion, this effect is often inherent due to imperfections in the manufacturing and assembly of the trap electrodes however it can also be caused by the buildup of stray charges on nearby dielectric surfaces [62]. The null positions of the oscillating and static fields are then given by the vectors  $r_{rf} = (0, 0, z)$  and  $r_{dc} = (x_{dc}, y_{dc}, 0)$  respectively. The trap potential from equation 2.68 is altered as

$$\begin{aligned} \Phi_{alt} = & A \cos(\Omega_{rf}t) (x^2 - y^2) \\ & - B \left[ (1 + \epsilon)(x - x_{dc})^2 + (1 - \epsilon)(y - y_{dc})^2 - 2z^2 \right]. \end{aligned} \quad (2.74)$$

An ion in a low-lying state which is confined by the potential above will experience

a harmonic pseudopotential that is shifted in position as

$$U_l = \frac{M}{2}(\omega_x^2(x - x_g)^2 + \omega_y^2(y - y_g)^2 + \omega_z^2 z^2), \quad (2.75)$$

where  $r_g = (x_g, y_g, 0)$  is the equilibrium position of the ion. The radial positions are given by

$$x_g = -\frac{2eB(1 + \epsilon)x_{dc}}{M\omega_x^2}, \quad (2.76)$$

$$y_g = -\frac{2eB(1 - \epsilon)y_{dc}}{M\omega_y^2}. \quad (2.77)$$

As before, the Rydberg ion polarizability introduces an additional harmonic potential, based on the average electric field strength at its position. This shift is again given by equation 2.71 and is centered on  $r_{rf}$  as the oscillating electric field remains the dominant contributor. The trapping frequencies are therefore altered according to equation 2.72. Crucially, the altered harmonic pseudopotential for the Rydberg state differs from that of the low-lying state and therefore the equilibrium position for the Rydberg ion is also shifted ( $r_R \neq r_g$ ). The Rydberg state pseudopotential is described by

$$U_R = \frac{M}{2}(\omega_x'^2(x - x_R)^2 + \omega_y'^2(y - y_R)^2 + \omega_z^2 z^2) + \delta \quad (2.78)$$

where the new radial positions are

$$x_R = \left(1 - \frac{2\alpha A^2}{M\omega_x^2}\right)^{-1} \quad (2.79)$$

$$y_R = \left(1 - \frac{2\alpha A^2}{M\omega_y^2}\right)^{-1}, \quad (2.80)$$

and the additional energy shift is

$$\delta = \frac{M}{2}(\omega_x^2 x_g^2 + \omega_y^2 y_g^2 - \omega_x'^2 x_R^2 - \omega_y'^2 y_R^2) \quad (2.81)$$

$$\approx -\alpha A^2(x_g^2 + y_g^2) \quad (2.82)$$

$$\approx -\alpha A^2(x_R^2 + y_R^2). \quad (2.83)$$

The approximations above are valid under the condition that  $2\alpha A^2 \ll M\omega_x^2$ , such that  $\delta$  is treated by perturbation theory as a quadratic Stark shift in exactly the

same manner as was considered in section 2.4.2. Thus the consequence of excitation to a Rydberg state when  $r_{rf} \neq r_{dc}$  is an altered trapping pseudopotential that is both Stark shifted and displaced from the trapping pseudopotential for an ion in a low-lying state (which is also displaced from the trap centre, but not by the same amount nor necessarily in the same direction, depending on the sign of  $\alpha$ ). The effects described in this section have been observed and characterized for a single trapped Rydberg ion in [54, 55]. Additional effects present for Rydberg states with permanent quadrupole moments have also been identified. Static resonance shifts occur due to the DC quadrupole field and coupling ( $\Delta m_j = \pm 2$ ) between Zeeman sublevels of a particular Rydberg state manifold can be driven by the RF field. Performing highly precise micromotion compensation is therefore a key factor in the development of Rydberg ion experiments; in chapter 8 we present a novel technique which can be used to achieve this goal.

# 3

## Experimental system

---

In this chapter the experimental system we use to trap and manipulate strontium ions is described in detail. This room-temperature setup was used for all of the experiments performed in this thesis. The focus of this chapter is on the hardware, such as the trap chamber, orientation of incoming beams and control of the individual laser systems (pulsing, frequency stabilisation and tuning). More detailed information on aspects related to the control of experiments, such as pulse sequencing and the user interface, are available in the following theses [74, 88].

### 3.1 Linear Paul trap

Our system uses a macroscopic linear Paul trap with a design similar to that shown in figure 2.1. A full schematic of the experimental setup is shown in figure 3.1. The distance from each of the radial electrodes to the trap axis is  $r_0 = 0.57\text{mm}$  and the distance between either endcap electrode and the trap centre is  $z_0 = 2.25\text{mm}$ . Endcap electrode voltages are set independently, typically in the range of  $\sim 100\text{V}$  up to  $\sim 2\text{kV}$ . The RF voltage applied to a pair of blade electrodes is initially supplied by a direct digital synthesizer ( $< 1\text{V}$ ) and passes through a 43dB amplifier<sup>1</sup> before entering a helical resonator that delivers a stable waveform to the trap. The final voltage on the blade electrodes is typically on the order of  $\sim 1\text{kV}$ . The significantly shorter distance between blade electrodes and the trap centre ensures that ions experience a stronger electric field in the x-y plane and are therefore tightly confined to form a linear string along the z-axis. Ion separation is dependent on the endcap electrode voltages and the size of the chain ( $\sim 5\mu\text{m}$  for typical operation). Forcing ions closer together may be advantageous for schemes that rely on direct interactions, as is the case when using Rydberg ions, meaning that the reduced distance leads to faster gate times. However, higher axial trapping frequencies also require higher laser powers for efficient cooling and especially for longer ion chains, necessitate the use of higher radial trapping frequencies to

---

<sup>1</sup>Minicircuits LZY-22+

maintain a 1D structure. This in turn leads to increased heat dissipation on the blade electrodes and therefore higher heating rates. It is also possible to create more condensed 2D structures by increasing the endcap electrode voltages for a fixed RF drive power, though the displacement of ions from the trap axis can cause additional problems in terms of excess micromotion and more demanding setups for single-ion addressing.

The trap is held in an ultra-high vacuum chamber currently at  $< 10^{-10}$  mbar which is maintained by an active ion-getter pump<sup>2</sup>. Figure 3.1 displays a schematic of the experimental setup including the various beam paths and readout equipment. The vacuum chamber and the addressing optics surrounding it are encased within a  $\sim 1\text{m}^3$  mu-metal box that shields the setup from disturbance due to external magnetic fields. The quantization axis is defined by a uniform magnetic field with strength  $B_0 = 3.6\text{G}$  that is produced by a pair of permanent magnets, more details on its configuration are available in the Master's thesis of Anders Lindberg [89]. Two additional pairs of Helmholtz coils, placed orthogonally to the quantization axis, are used to compensate any misalignment between the quantization axis and the trap axis. The coils are driven by custom-made stabilized current drivers operating in the mA range, the resulting field strengths are on the order of mT. Additional steps are taken to minimize all possible sources of magnetic field noise within the mu-metal shielding (such as the use of plastic isolators for mirror mounts and other non-magnetic opto-mechanical components), however the current experimental setup requires the use of certain electronic components within the inner chamber of the mu-metal box (primarily acousto-optic deflectors). Further details about the material properties and initial setup of the trap and vacuum chamber are available in the Doctoral thesis of Fabian Pokorny [90].

---

<sup>2</sup>SAES Getters NEX Torr D 100-5

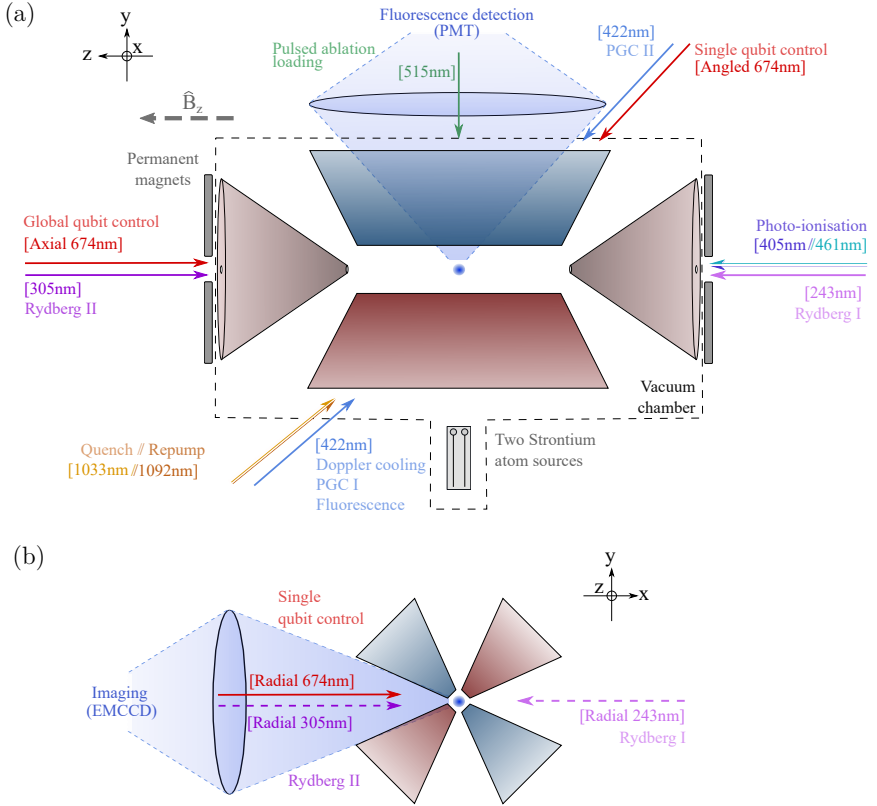


FIG. 3.1: Simplified schematic of the linear Paul trap and the standard configuration of incoming laser beams. Electrode polarity is indicated by colour (red for positive and blue for negative) at a particular instant during the radio-frequency oscillation of the trap drive. (a) A side view of the trap, perpendicular to the quantisation axis. Two of the four blade electrodes are shown. In the cases where multiple beams of different wavelength are present at the same optical access port, laser beams are overlapped in photonic crystal fibers before being delivered to focusing optics close to the trap chamber. The 422nm and angled 674nm beams above the trap are the only exception; they are instead delivered by separate single-mode fibers and overlapped using optics close to the trap chamber. PGC refers to beams used for polarisation gradient cooling. (b) An end-to-end view in which the endcap electrodes are omitted for clarity. Dashed arrows indicate an alternate setup of Rydberg lasers, replacing those in the top figure to allow for the selective Rydberg excitation of one or more ions in a chain. In this case the 674nm and 305nm beams are delivered by separate fibers and overlapped by optics close to the trap chamber. The 243nm beam is delivered entirely via free-space optics to reduce losses incurred by the use of photonic crystal fibers. The permanent magnetic field is also rotated to the radial direction, although this is not depicted on the figure.

## 3.2 Laser systems

The ions trapped in our experiment are  $^{88}\text{Sr}^+$ , an alkali earth metal that was chosen because there is one valence electron after ionisation available for qubit operations and because Rydberg excitation is possible using a two-photon scheme that does not require vacuum ultraviolet laser light (all lasers are operated with  $\lambda > 200\text{nm}$ ). All transitions between low-lying states also occur at frequencies accessible with commercial laser diodes. A simplified level scheme for  $^{88}\text{Sr}^+$  detailing all of the relevant transitions is shown in figure 3.2. Atoms are loaded into the trap via ablation of a  $^{88}\text{Sr}$  sample using a 515nm pulsed diode laser<sup>3</sup>, details on the setup and installation are given in the masters thesis of Andreas Pöschl [88]. The  $^{88}\text{Sr}$  source is placed beneath the trap so that ablated atoms travelling upwards can be ionised in a two-step process by co-propagating 461nm<sup>4</sup> and 405nm<sup>5</sup> lasers which are directed along the trap axis. Ionized atoms are then cooled using red-detuned 422nm light<sup>6</sup> which drives the transition between the ground state  $5\text{S}_{1/2}$  and the short-lived excited state  $5\text{P}_{1/2}$  (shown by the light blue arrow in figure 3.2). Scattering via this transition is also used to read out the ion's electronic state with high efficiency in a process known as electron shelving [71]. A small fraction of the emitted photons are sent to a photomultiplier tube<sup>7</sup> which is triggered so that the number of detection events during a measurement is recorded; another small fraction are directed towards an EMCCD camera<sup>8</sup> so that individual ions or crystal structures can be imaged in situ. The 422nm laser can also be used for polarisation gradient cooling (PGC) by adding a second beam that is counter-propagating and ensuring that the two beams have orthogonal linear polarisations, equal intensities and equal detunings [66].

During Doppler cooling and state readout, decay from the state  $5\text{P}_{1/2}$  brings population to the metastable state  $4\text{D}_{3/2}$  in  $\sim 6\%$  of cases. Here the system is in a dark state and a 1092nm repump laser<sup>9</sup> is therefore switched on concurrently to drive population back to the short-lived excited state. Logical qubit states  $|1\rangle$  and  $|0\rangle$  are assigned to the ground state  $5\text{S}_{1/2}$  and metastable excited state  $4\text{D}_{5/2}$ . The quadrupole transition (shown by the red arrow in fig 3.2) is driven by a 674nm laser<sup>10</sup> that can enter the trap via one (or multiple simultaneously) of three beam paths. The 1033nm laser<sup>11</sup> drives the "quench" transition from  $4\text{D}_{5/2}$

---

<sup>3</sup>Coherent Flare-NX

<sup>4</sup>Toptica DL pro

<sup>5</sup>RGB photonics  $\lambda$  beam wavelock

<sup>6</sup>Toptica DL pro

<sup>7</sup>Hamamatsu Photonics H10682-210

<sup>8</sup>Andor iXon3 897

<sup>9</sup>Toptica DL pro

<sup>10</sup>Toptica TA pro

<sup>11</sup>Toptica DL pro

to  $5P_{3/2}$  to expedite returning population to the ground state. By addressing certain sublevels within the Zeeman manifold of the quadrupole transition, the combination of 674nm light, 1033nm light and spontaneous decay from  $5P_{3/2}$  to  $5S_{1/2}$  forms a closed cycle which can be used for state manipulation and resolved sideband cooling [71]. By addressing other sublevels the same combination can also form an open cycle for use in state preparation via optical pumping. Thus the combination of lasers described so far is sufficient to perform effective cooling and any single qubit operation on a trapped ion. More details on the specific decay rates of each level are given in [74]. Each of the lasers mentioned above (aside from the 405nm, 461nm and 515nm) is frequency shifted using acousto-optic modulators<sup>12</sup> (AOM) in either single- or double-pass configurations so that transitions can be driven between specific Zeeman sublevels or via motional sidebands. The AOM signals are provided by direct digital synthesisers (DDS) or from the in-house designed pulse box (Innsbruck design); this also allows for the laser light from a continuous wave source (which applies to all but the 515nm) to be sent onto the ion with a user-defined pulse length.

Rydberg excitation is performed via a two-photon transition (demonstrated by the purple arrows in figure 3.2) using counter-propagating beams. Light at 243nm is used to drive the transition between the metastable state  $4D_{5/2}$  and an intermediate state  $6P_{3/2}$ . From there a 305-310nm tunable laser is used to transfer population to a Rydberg state  $n_R S_{1/2}$  within the range  $26 < n_R < 60$ , theoretically the second excitation stage should be able to transfer population to any state with  $n > 26$  up to the second ionisation limit; in reality however there are a number of technical constraints that have so far prevented excitation beyond  $n = 60$  [90]. To avoid scattering from the short-lived intermediate state, both the 243nm and 305-310nm lasers are detuned by an equal and opposite amount ( $\Delta_{243} = -\Delta_{305}$  with  $\Delta_{305} \approx +80\text{MHz}$ ). Coupling from  $n_R S_{1/2}$  to Rydberg states with  $l > 0$  in the range  $43 < n_R < 60$  is achieved using a tunable microwave field<sup>13</sup> (shown in light green in fig 3.2) that operates in either the WR15-band (50-75GHz) or the WR8-band (90-140GHz). The intermediate state  $6P_{3/2}$  decays rapidly compared to either the metastable or Rydberg states, efficient population transfer from  $4D_{5/2} \rightarrow n_R S_{1/2}$  therefore requires that  $\Omega_{305} \gg \Gamma_{int}$ , where  $\Omega_{305}$  is the Rabi frequency of the 305-310nm laser and  $\Gamma_{int} = 4.9\text{MHz}$  is the decay rate of  $6P_{3/2}$ . Coherent ultraviolet laser light at 243nm is produced by two stages of second harmonic frequency generation. The process begins with a commercial diode laser at 970nm<sup>14</sup> which is twice converted using a lithium triborate (LTO) crystal and a barium borate (BBO) crystal in the first and second stages respectively. The 305-310nm laser

---

<sup>12</sup>Gooch & Housego / Isomet

<sup>13</sup>Anritzu MG3690C / Virginia Diodes Inc.

<sup>14</sup>Toptica FHG

light is also produced in a two-stage process. The first involves sum frequency generation between one fixed wavelength fiber laser at 1550nm<sup>15</sup> and one tunable diode laser at 1010nm<sup>16</sup>, the two are overlapped on a periodically-poled lithium niobate (PPLN) crystal to produce light at 610nm. The second stage involves second harmonic generation of the 610nm light using a lithium borate (LBO) crystal<sup>17</sup>. More technical details for the setup of the two Rydberg excitation lasers can be found in the Master's thesis of Christine Maier [91].

The 422nm, 1033nm and 1092nm lasers are stabilised by a lock-in method to reference cavities with finesse  $\sim 1000$  (built in-house), the corresponding laser linewidths are  $\sim 2\pi \times 100\text{kHz}$ . The 610nm and 970nm lasers are locked via the Pound-Drever-Hall (PDH) technique [92] to a commercial reference cavity<sup>18</sup> with a finesse  $\sim 20,000$  resulting in laser linewidths of  $\sim 2\pi \times 10\text{kHz}$  [74]. The 674nm laser which is used for qubit manipulation is PDH-locked to a commercial reference cavity<sup>19</sup> with a finesse of  $\sim 100,000$  resulting in a stabilised laser linewidth of  $\sim 2\pi \times 600\text{Hz}$  [93].

---

<sup>15</sup>NKT Koheras Basic amplified by a Manlight ML10-EYFA-CW-SLM-P-TKS

<sup>16</sup>Toptica TA pro

<sup>17</sup>Toptica SHG pro

<sup>18</sup>Stable Laser Systems

<sup>19</sup>Stable Laser Systems / ATFilms

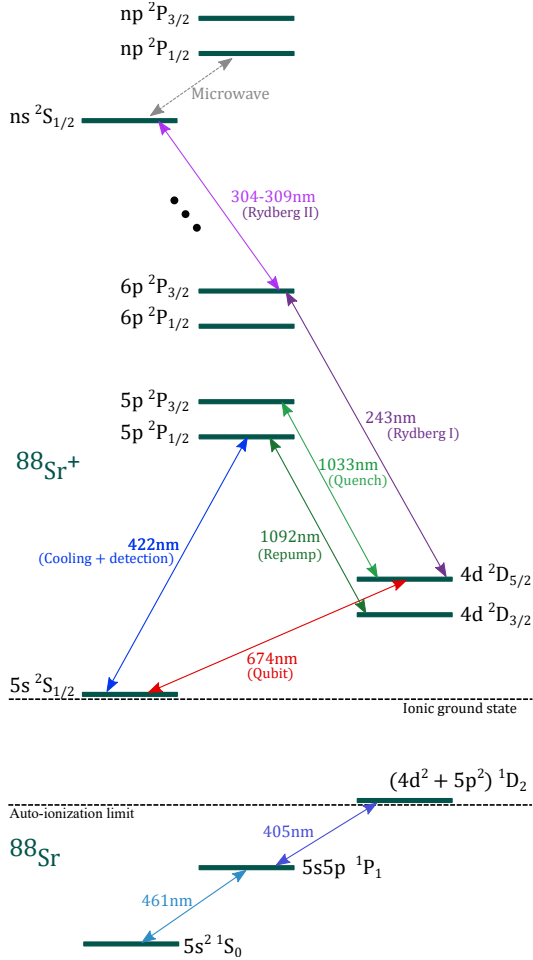


FIG. 3.2: Simplified level scheme for  $^{88}\text{Sr}^+$  including the two-step photo-ionization that is performed during ion loading. Logical qubit states are assigned to certain Zeeman sublevels of the  $5S_{1/2}$  ground state and  $4D_{5/2}$  metastable state. Transitions between low-lying states are often driven close to resonance; two-step Rydberg excitation requires that the intermediate state  $6P_{3/2}$  is not populated so both the 243nm and 304-309nm lasers are detuned from their respective transitions whilst maintaining the two-photon resonance between  $4D_{5/2}$  and  $nS_{1/2}$ .

# 4

## Phononic bright and dark states: Investigating multi-mode interference with a single trapped ion

---

The interaction between the internal electronic and external motional states of a single trapped ion can be engineered to closely resemble that of a neutral atom placed within a cavity. When only one cavity mode interacts resonantly with the atom, the dynamics are well described by the conventional Jaynes-Cummings Hamiltonian. Adaptations of this relatively simple setup typically involve the addition of more atoms, resulting in collective interactions described by the Dicke model. Similar collective effects are, however, also realizable with a single atom by instead increasing the number of field modes involved in the interaction. In this case the observed light-matter interactions and interference phenomena are inextricably linked. With the results presented in this chapter, we demonstrate a novel interpretation of the concept of interference, based on the formation of collective bosonic states. By describing interference effects as a form of multi-mode coupling between light and matter we show that both classical and non-classical wave properties can be attributed to the purely quantum-mechanical collective states. We perform this analysis using a single trapped ion and two motional modes to effectively simulate the simultaneous coupling of an atom to two independent cavity modes. This work marks the first time that the interaction of such collective states has been experimentally observed. The paper is currently available on arxiv [94], my contributions are listed in section 1.1.1.

# 5

## Single-shot measurements of phonon number states using the Autler-Townes effect

---

With a high-dimensional Hilbert space and tunable couplings to specific energy levels, the motional state of a trapped ion is a valuable tool for various forms of quantum computation and metrology. Efficient and accurate detection of motional states is therefore an integral component of many ion trap experiments. The most conventional method of detection involves driving Rabi oscillations on motional sideband transitions and extracting the phonon number from the oscillation rate. In this case a bare minimum of one full period needs to be observed in order to obtain an accurate measurement but typically, and especially when the system does not reside in a single Fock state, multiple periods of oscillation on both red and blue motional sidebands are required for the state to be reliably determined. The complete detection sequence of this method also requires the state to be reinitialized after each individual measurement, lengthening the overall detection time. Other, more efficient methods have been proposed and demonstrated experimentally but in each case, re-initialization after each measurement remains a potential issue. In the paper presented in this chapter a novel scheme for motional state detection, based on the Autler-Townes effect, is presented. The main advantage of this scheme is that it can be configured to offer either single-shot detection or non-demolition measurement of motional Fock states. In the former case, each Fock state can be checked sequentially via a series of pulses and the state is only disturbed by a positive result, such that reinitialization is only required when the correct Fock state is identified. In the latter case the reverse is true, negative results cause the destruction of the motional state but a positive result leaves it untouched; this allows for efficient verification and continued use in the event that the prepared state was known prior to the measurement being performed. The results of this work are published in [95], my contributions are listed in section 1.1.2.

# 6 Motional-state analysis of a trapped ion by ultranarrowband composite pulses

---

In chapter 5 a novel detection scheme for measuring the motional state of trapped ions (and other equivalent systems) was introduced. In this chapter a second novel detection scheme is presented, based on the use of composite pulse sequences. The key advantage of this scheme over other detection methods is the wide range of applicability. The efficient, single-shot detection of the Autler-Townes effect is generally limited to the lower phonon-number states, for which the differences in phonon-number-dependent coupling strength are more pronounced. Driving Rabi oscillations typically allows for the probing of higher Fock states but the approximations which are made to accurately fit the data, and extract from it the correct motional state, are restricted to work only within the Lamb-Dicke regime (see section 2.3.7 for more details). On the other hand, with the use of ultranarrowband composite pulses, it is possible to apply the same detection technique both well-within and well-outside of the Lamb-Dicke regime whilst maintaining a high level of accuracy in the measurement results. The paper is published in [96], my contributions are listed in section 1.1.4.

# 7 Observation of second- and higher-order electric quadrupole interactions with an atomic ion

---

Owing to their large polarizabilities, trapped Rydberg ions make effective electric field sensors. Studies of the interaction between individual atomic ions and trapping fields are particularly important in the field of precision spectroscopy, in order to allow for the compensation of frequency shifts in atomic clocks [80]. Higher-order effects, due to quadrupole and higher multi-pole interactions are typically neglected outside of studies of molecular trapped ions [97] but will need to be considered as technological improvements lead to smaller frequency uncertainties. Trapped Rydberg ions therefore offer a useful tool to probe this regime for single atomic ions in advance of even the highest precision atomic clocks [98]. For our experiment, the use of Rydberg states to perform quantum gate operations also necessitates a thorough understanding of the interaction with the trapping field. Since Rydberg interaction strengths are ultimately limited by the size of the induced dipoles, paired with the fact that vanishing polarizability states may be required when working with longer ion crystals (see section 2.4.4 for details), the need to excite to higher Rydberg states is an important consideration for future experimental work. Consequently the effects due to ion's quadrupole polarizability will become more pronounced; since these are the lowest-order effects that are intrinsically unavoidable with the current system it is vital that we can reliably calculate and measure them. In this chapter these effects are characterized for multiple Rydberg states, we observe static resonance shifts and the emergence of various Floquet sidebands in the Rydberg excitation spectra. We also demonstrate a new coherent spectroscopy technique that allows Rydberg states to be probed with minimal loss due to double ionization. This work was published in [99], my contributions are listed in section 1.1.3.

## 8

# Micromotion minimization using Ramsey interferometry

---

In the previous chapters we have demonstrated novel techniques for motional state detection and Rydberg state spectroscopy and we have highlighted the advantages that they offer over more conventional schemes. In this chapter we introduce a novel technique for micromotion compensation, which is another vital aspect of almost all trapped ion experiments. Excess micromotion is present in the system when the equilibrium position of the ion is shifted by stray charges away from the axis of the RF field null. The size of the shift depends on both the magnitude of the stray field and the stiffness of the trap (i.e. the strength of the RF field gradient). Consequently, the movement of the ion due to changes in the trap stiffness can be used as a measure of excess micromotion. The method presented in this chapter employs Ramsey interferometry of a single ion during a period over which the trap stiffness is abruptly switched between different levels. The movement of the ion is then probed by the observation of phase shifts in the Ramsey pulse sequence. This method has the advantage of being technically simple, whilst allowing for the efficient detection of stray electric fields to a greater precision than can be achieved with other state-of-the-art techniques. Combining this method with the conventional method of probing sidebands caused by the first-order Doppler shift [62] also has the advantage that compensation of orthogonal motional modes (in the 2D plane perpendicular to a linear Paul trap axis) can be performed with a single probe beam that is parallel with only one of the micromotion axes. This means that a single beam allows for completely independent compensation of both horizontal and vertical micromotion. In this chapter we demonstrate the effectiveness of this technique in both 2D and 3D micromotion minimization and show how it can be made robust to small errors in the pulse area and frequency stability of the probe laser. We also show how the utility of the scheme can be expanded by relating it to quantum clock synchronization protocols. This work was published in [100], my contributions are listed in section 1.1.5.

# 9

## Summary and outlook

---

In this thesis several works focusing on the application and detection of trapped ion motion have been presented. We have used multi-mode phononic operations to simulate coupling between light and matter and provided the first experimental evidence of a novel link between such interactions and the concept of interference. Notably, despite being based on the formation of specific quantum states, this classification scheme can be used to accurately describe the coupling of both quantum and classically-interfering fields alike. The multi-mode phononic states employed in this work have also not previously been directly observed in a trapped ion system and we have highlighted the potential use of these states in terms of quantum computation. We have also demonstrated how the Autler-Townes effect can be used to obtain both highly-efficient and accurate measurements of the motional state of a single trapped ion. This novel detection scheme offers certain advantages over more conventional methods, such as the ability to perform single-shot measurements of arbitrary motional states or non-demolition measurements of Fock states. A second scheme is also presented in which composite pulses offer an exceptionally wide range of accurate motional state detection, either for highly-precise measurements of relatively low phonon numbers or for the accurate estimation of motional states well beyond the Lamb-Dicke regime.

Adding to this expanded quantum toolkit, we also presented a new method for micromotion minimisation in a trapped ion system. By using Ramsey interferometry it is possible to outperform more conventional methods of micromotion compensation in terms of both accuracy and speed. Finally, we have shown how the quadrupole polarisability of Rydberg states can be precisely measured using a trapped ion system. We have examined the action of the trapping fields on a single ion excited to a Rydberg state and verified how such effects can be theoretically calculated; this is an important step in the development of a viable quantum information processor based on the use of trapped Rydberg ions. Although the works presented in this thesis primarily concern low-lying atomic states and are therefore more broadly applicable in terms of ion trap systems, the underlying

goal of this research is in the advancement of the trapped Rydberg ion system on which all of the experiments were performed. With the exception of the bright and dark states, in which the main motivation behind the experimental work was a theoretical development in the field of quantum optics, each of the experiments described above offers direct benefits to the enhancement of our system. Recently a number of other steps towards this goal have also been made, those in which I was involved are detailed below:

- **Single-ion addressing of the qubit laser**

As mentioned in Sec. 1 a setup for single-ion addressing was recently installed in the experimental system. By altering the radio-frequency input of a single Acousto-Optic Deflector (AOD)<sup>1</sup> a qubit laser beam directed perpendicular to the trap axis is able to individually address any one of a linear chain of ions over a certain range. The level of unwanted excitation of neighbouring ions is determined by the size of the beam waist at the ion position, the spacing between ions and either the amplitude or power of the incoming light field, depending on whether the addressed ion is excited directly or Stark shifted during a Ramsey sequence of global pulses [68]. Although not currently a limiting factor in Rydberg ion entanglement operations, being able to individually excite select pairs of ions to energy levels which can then be coupled to Rydberg states, whilst limiting the unwanted excitation of all other ions will lead to a reduction in gate errors in future experiments. The use of an AOD also allows for much faster selection of ions than what can be achieved by, for example, shuttling the ions into the path of a fixed laser beam. The speed of such selections can be improved further by using mixed RF signals at the AOD input such that two or more addressing beams can be produced simultaneously, at the time of writing this step has not yet been tested.

- **Improved alignment and single-ion addressing of the Rydberg lasers**

The initial setup of the two-stage Rydberg excitation had the beams propagating along the trap axis in opposite directions. For the two-step process, counter-propagating beams are advantageous due to the fact that recoil effects during the absorption of high-energy UV photons are largely mitigated. This does however, provide additional technical challenges in terms of beam delivery and alignment. Orientation along the trap axis was originally easier to implement and also placed a limit on the minimum waists of the beams that simplified alignment; in this case the limit is a result of the axial beams passing through small holes in the endcap electrodes, reducing the numerical

---

<sup>1</sup>Gooch & Housego

aperture of the optical setup when compared with those available to beams at other optical access ports. This orientation also has the advantage that all ions in a linear chain are simultaneously addressed by the Rydberg lasers such that any differences in laser power at the individual ion positions are negligible.

On the other hand, the lack of individual ion addressing means that selection of Rydberg ions is performed solely by the qubit laser (as only one of the qubit states is coupled by the first-stage Rydberg laser), this in turn means that unwanted Rydberg excitation will occur as a result of errors in the rotation of single qubits. The consequence would be a reduction in fidelity of Rydberg-interaction based gate schemes due to the additional ions becoming entangled with the targeted pair. A second key disadvantage of the axial orientation, which becomes increasingly problematic as ion strings increase in length, is the Doppler effects that occur as a result of ion motion. To maintain a 1D chain when more ions are loaded into the trap, the axial trap frequency has to be reduced. This, coupled with the fact that effective cooling also becomes more difficult for longer ion chains and the fact that UV photons require more stringent conditions to meet the Lamb-Dicke criterion, means that the Doppler effects (in this case an unwanted coupling between ion motion and the qubit states as well as a broadening of the Rydberg transition) become a significant issue for entanglement operations [61].

The best way to solve these issues is to change the orientation of the counter-propagating Rydberg beams so that they are instead aligned perpendicular to the trap axis. Doing so allows for individual ion addressing provided the focus of the beam is sufficiently narrow and removes the majority of the detrimental Doppler effects since the radial trapping frequencies are ideally not constrained by the number of ions in a chain. The new radial orientation also allows for both beams to be more tightly focused, allowing for higher intensities at the ion positions. For the dipole-dipole interaction Rydberg gate which has already been demonstrated in our system [50], higher intensities allow for faster Rydberg excitation via stimulated Raman adiabatic passage (STIRAP), which is the main determinant of the overall gate speed. It should be noted that the permanent magnetic field defining the quantisation axis must also be rotated to the radial direction to ensure the most efficient transfer during Rydberg excitation. Pure circular polarisations are required of the two UV beams to prevent mixing of the Zeeman sublevels of the three levels involved  $\{4D_{5/2}, 6P_{3/2}, nS_{1/2}\}$  [74]. At the time of writing these new setups have been implemented, despite the significant power loss ( $\sim 50\%$ ) that occurs with optimal coupling through each of the AODs, a

notable increase in intensity for both beams has been observed as a result of the improved focusing. The full capability of the single-ion addressing, including the selective excitation of any pair of ions within a chain and, as with the qubit laser, the use of mixed frequency RF drives on the AODs, will be realised in future experiments.

There are also a number of more significant improvements which are currently either in development or consideration for future iterations of the experimental system:

- **Utilising a cryogenic ion trap system**

All of the experiments featured in this thesis were performed on a room-temperature setup. For those experiments strictly involving low-lying states the motional heating rates of our macroscopic linear Paul trap are sufficiently low so as to be neglected in most cases and motional dephasing rates are several orders of magnitude smaller than what we observe for any optical transition. A cryogenic setup, with the same trap design, would further improve these quantities but more significantly benefit experiments making use of Rydberg states. One of the reasons Rydberg ions make for attractive mediators in entanglement operations is their long lifetime (typically on the order of several  $\mu\text{s}$  for principle quantum numbers of  $n \sim 50$ ). In the absence of other external factors radiative decay from the Rydberg state most commonly occurs via transitions to low-lying states, due to the higher mode volume for UV-wavelength photons. The natural lifetime therefore scales as  $n^3$ . In the presence of black-body radiation, the narrow transitions between Rydberg states can be driven at a rate exceeding the natural decay, this leads to a reduction in the Rydberg state lifetime such that it scales as  $n^2$  [101]. The reduced lifetime places a limit on the available fidelity of Rydberg-interaction-based gate schemes that would be overcome with the use of a cryogenic system.

Additionally ion loss by double-ionisation whilst in the Rydberg state is currently one of the main technical challenges limiting the efficient performance of Rydberg experiments. In cases where this occurs the ion must be ejected from the trap; presently this means that all ions in a chain must also be ejected and reloaded. This issue can be resolved by altering the trap settings temporarily to a configuration in which stable trapping parameters are achieved for singly-charged but not doubly-charged ions [61]. However, frequent reloading of ions by ablating a Strontium sample can quickly lead to a build-up of so-called dark ions (in the case of Strontium and with a free-running photoionization laser loading is not isotope selective [88]). Although

several methods exist to remove incorrect isotopes from a linear Paul trap [102, 103], the overall result is still an increase in the time and complexity of the loading procedure. Even with rapid ablation loading, optimised loading times are still several orders of magnitude longer than a typical run of an experimental sequence (including initialisation and ion readout) such that a significant amount of time in any experiment involving Rydberg ions is dedicated to reloading. It has been suggested that black-body radiation may contribute to an increased rate of ion loss by double-ionisation [50, 104]; a cryogenic system may therefore allow for Rydberg experiments to be performed much faster and more reliably than with the current setup. At the time of writing a cryogenic setup is in development.

- **Faster loading using a Magneto-optical trap**

As mentioned above, ion loading, particularly with the use of Rydberg states, can be a time-consuming process and one that will likely pose a limit on scalability when it comes to performing lengthier computations. Segmented and modular trap designs can circumvent this issue by making use of dedicated loading and storage zones; efficient replacement of qubits is then possible by shuttling ions out of the isolated trapping potentials of a storage zone and into an active zone where the computation takes place [39]. Another method is to load from a reservoir of neutral atoms held by a magneto-optical trap (MOT). When used in combination with a cryogenic trap system and conventional photo-ionisation techniques ions can be efficiently loaded from a cooled atomic beam that is directed through the trapping region. MOT loading has been shown to enable very high loading rates with site-selectivity (via single-ion addressing of the photo-ionisation beams) and minimal disturbance to neighbouring ions already contained within the trap [105].

- **Switching to microfabricated planar chip traps**

Beyond ion loading and the efficiency with which quantum operations can be performed, the physical size and energy requirement of quantum devices is another scalability issue that needs to be addressed. Microfabricated ion trap systems offer significant advantages in terms of compactness, efficient production and integration with other on-chip technologies. Extensive research on integrated photonics is ongoing at various institutions worldwide and single chips capable of delivering multiple wavelengths to cool, control and detect trapped Strontium ions have already been realised [106]. Other chip devices featuring an all-electrical control of trapped ion qubits have also recently been demonstrated [18].

Trapped Rydberg ions have yet to be realised in a chip trap system and

there are a number of key considerations that will need to be experimentally tested. Planar microfabricated traps often feature shallower trap depths than macroscopic linear Paul traps as well as smaller distances between the trapped ions and nearby surfaces. As a result, trapped particles are typically more severely affected by electric field noise and the buildup of stray charges; this often leads to higher rates of motional heating. These effects are likely to be even more pronounced for Rydberg ions as a consequence of their extreme sensitivity to electric fields. Comprehensive study of these effects and potential mitigation either by trap design or by other compensatory techniques is therefore going to be a major milestone in the advancement of trapped Rydberg ion quantum technologies. At the time of writing, a chip trap is in development and will be tested on the cryogenic system as part of an ongoing project.

# Bibliography

- [1] J. I. Cirac and P. Zoller, “Quantum computations with cold trapped ions”, *Physical Review Letters* **74**, 4091 (1995).
- [2] C. J. Ballance, T. P. Harty, N. M. Linke, M. A. Sepiol, and D. M. Lucas, “High-Fidelity Quantum Logic Gates Using Trapped-Ion Hyperfine Qubits”, *Physical Review Letters* **117**, 060504 (2016).
- [3] P. Wang, C. Y. Luan, M. Qiao, M. Um, J. Zhang, Y. Wang, X. Yuan, M. Gu, J. Zhang, and K. Kim, “Single ion qubit with estimated coherence time exceeding one hour”, *Nature Communications* **12**, 233 (2021).
- [4] C. R. Clark, *et al.*, “High-Fidelity Bell-State Preparation with  $^{40}\text{Ca}^+$  Optical Qubits”, *Phys. Rev. Lett.* **127**, 130505 (2021).
- [5] S. M. Brewer, J.-S. Chen, A. M. Hankin, E. R. Clements, C. W. Chou, D. J. Wineland, D. B. Hume, and D. R. Leibbrandt, “ $^{27}\text{Al}^+$  Quantum-Logic Clock with a Systematic Uncertainty below  $10^{-18}$ ”, *Phys. Rev. Lett.* **123**, 033201 (2019).
- [6] K. A. Gilmore, M. Affolter, R. J. Lewis-Swan, D. Barberena, E. Jordan, A. M. Rey, and J. J. Bollinger, “Quantum-enhanced sensing of displacements and electric fields with two-dimensional trapped-ion crystals”, *Science* **373**, 673 (2021).
- [7] F. Bonus, C. Knapp, C. H. Valahu, M. Mironiuc, S. Weidt, and W. K. Hensinger, “Ultrasensitive single-ion electrometry in a magnetic field gradient”, [arXiv:2406.08424](https://arxiv.org/abs/2406.08424) (2024), [10.48550/arXiv.2406.0842](https://arxiv.org/abs/10.48550/arXiv.2406.0842).
- [8] F. Wolf, C. Shi, J. C. Heip, M. Gessner, L. Pezzè, A. Smerzi, M. Schulte, K. Hammerer, and P. O. Schmidt, “Motional Fock states for quantum-enhanced amplitude and phase measurements with trapped ions”, *Nature communications* **10**, 2929 (2019).
- [9] M. Johanning, A. F. Varón, and C. Wunderlich, “Quantum simulations with

- cold trapped ions”, *Journal of Physics B: Atomic, Molecular and Optical Physics* **42**, 154009 (2009).
- [10] R. Blatt and C. F. Roos, “Quantum simulations with trapped ions”, *Nature Physics* **8**, 277 (2012).
- [11] C. Schneider, D. Porras, and T. Schaetz, “Experimental quantum simulations of many-body physics with trapped ions”, *Reports on Progress in Physics* **75**, 024401 (2012).
- [12] J. T. Barreiro, M. Müller, P. Schindler, D. Nigg, T. Monz, M. Chwalla, M. Hennrich, C. F. Roos, P. Zoller, and R. Blatt, “An open-system quantum simulator with trapped ions”, *Nature* **470**, 486 (2011).
- [13] W. Paul, “Electromagnetic traps for charged and neutral particles (Nobel lecture)”, *Angewandte Chemie International Edition in English* **29**, 739–748 (1990).
- [14] M. E. Beverland, P. Murali, M. Troyer, K. M. Svore, T. Hoefler, V. Kliuchnikov, G. H. Low, M. Soeken, A. Sundaram, and A. Vaschillo, “Assessing requirements to scale to practical quantum advantage” (2022).
- [15] R. Lechner, C. Maier, C. Hempel, P. Jurcevic, B. P. Lanyon, T. Monz, M. Brownnutt, R. Blatt, and C. F. Roos, “Electromagnetically-induced-transparency ground-state cooling of long ion strings”, *Physical Review A* **93**, 053401 (2016).
- [16] T. Feldker, H. FÜRST, H. Hirzler, N. Ewald, M. Mazzanti, D. Wiater, M. Tomza, and R. Gerritsma, “Buffer gas cooling of a trapped ion to the quantum regime”, *Nature Physics* **16**, 413 (2020).
- [17] S. D. Fallek, V. S. Sandhu, R. A. McGill, J. M. Gray, H. N. Tinkey, C. R. Clark, and K. R. Brown, “Rapid exchange cooling with trapped ions”, *Nature Communications* **15**, 1089 (2024).
- [18] C. M. Löschnauer, *et al.*, “Scalable, high-fidelity all-electronic control of trapped-ion qubits” (2024), [arXiv:2407.07694](https://arxiv.org/abs/2407.07694) .
- [19] R. Srinivas, *et al.*, “High-fidelity laser-free universal control of trapped ion qubits”, *Nature* **597**, 209 (2021).
- [20] S. Weidt, J. Randall, S. Webster, K. Lake, A. Webb, I. Cohen, T. Navickas, B. Lekitsch, A. Retzker, and W. Hensinger, “Trapped-ion quantum logic with

- global radiation fields”, *Physical review letters* **117**, 220501 (2016).
- [21] A. Sørensen and K. Mølmer, “Quantum computation with ions in thermal motion”, *Physical Review Letters* **82**, 1971 (1999).
- [22] D. Leibfried, *et al.*, “Experimental demonstration of a robust, high-fidelity geometric two ion-qubit phase gate”, *Nature* **422**, 412–415 (2003).
- [23] K. Kim, M. S. Chang, R. Islam, S. Korenblit, L. M. Duan, and C. Monroe, “Entanglement and Tunable Spin-Spin Couplings between Trapped Ions Using Multiple Transverse Modes”, *Physical Review Letters* **103**, 120502 (2009).
- [24] M. Um, J. Zhang, D. Lv, Y. Lu, S. An, J.-N. Zhang, H. Nha, M. Kim, and K. Kim, “Phonon arithmetic in a trapped ion system”, *Nature communications* **7**, 11410 (2016).
- [25] W. Chen, *et al.*, “Scalable and programmable phononic network with trapped ions”, *Nature Physics* **19**, 877–883 (2023).
- [26] P. W. Shor *Fault-tolerant quantum computation* (Proceedings of 37th conference on foundations of computer science, 1996) pp. 56–65.
- [27] A. M. Steane, “Efficient fault-tolerant quantum computing”, *Nature* **399**, 124–126 (1999).
- [28] D. Gottesman *An introduction to quantum error correction and fault-tolerant quantum computation*, Vol. 68 (Quantum information science and its contributions to mathematics, Proceedings of Symposia in Applied Mathematics, 2010) pp. 13–58.
- [29] P. Schindler, J. T. Barreiro, T. Monz, V. Nebendahl, D. Nigg, M. Chwalla, M. Hennrich, and R. Blatt, “Experimental Repetitive Quantum Error Correction”, *Science* **332**, 1059–1061 (2011).
- [30] D. Nigg, M. Müller, E. A. Martinez, P. Schindler, M. Hennrich, T. Monz, M. A. Martin-Delgado, and R. Blatt, “Quantum computations on a topologically encoded qubit”, *Science* **345**, 302–305 (2014).
- [31] N. M. Linke, M. Gutierrez, K. A. Landsman, C. Figgatt, S. Debnath, K. R. Brown, and C. Monroe, “Fault-tolerant quantum error detection”, *Science Advances* **3**, e1701074 (2017).
- [32] L. Egan, *et al.*, “Fault-tolerant control of an error-corrected qubit”, *Nature*

- 598**, 281–286 (2021).
- [33] L. Postler, *et al.*, “Demonstration of fault-tolerant universal quantum gate operations”, *Nature* **605**, 675–680 (2022).
- [34] A. Erhard, *et al.*, “Entangling logical qubits with lattice surgery”, *Nature* **589**, 220–224 (2021).
- [35] Y. Chen, *et al.*, “Qubit architecture with high coherence and fast tunable coupling”, *Physical Review Letters* **113**, 220502 (2014).
- [36] D. J. Wineland, C. Monroe, W. M. Itano, D. Leibfried, B. E. King, and D. M. Meekhof, “Experimental issues in coherent quantum-state manipulation of trapped atomic ions”, *Journal of research of the National Institute of Standards and Technology* **103**, 259–328 (1998).
- [37] D. Kielpinski, C. Monroe, and D. J. Wineland, “Architecture for a large-scale ion-trap quantum computer”, *Nature* **417**, 709–711 (2002).
- [38] B. Lekitsch, S. Weidt, A. G. Fowler, K. Mølmer, S. J. Devitt, C. Wunderlich, and W. K. Hensinger, “Blueprint for a microwave trapped ion quantum computer”, *Science Advances* **3**, e1601540 (2017).
- [39] J. M. Pino, *et al.*, “Demonstration of the trapped-ion quantum CCD computer architecture”, *Nature* **592**, 209–213 (2021).
- [40] C. Monroe and J. Kim, “Scaling the ion trap quantum processor”, *Science* **339**, 1164–1169 (2013).
- [41] C. Monroe, R. Raussendorf, A. Ruthven, K. R. Brown, P. Maunz, L.-M. Duan, and J. Kim, “Large-scale modular quantum-computer architecture with atomic memory and photonic interconnects”, *Physical Review A* **89**, 022317 (2014).
- [42] V. Krutyanskiy, *et al.*, “Entanglement of trapped-ion qubits separated by 230 meters”, *Physical Review Letters* **130**, 050803 (2023).
- [43] W. Li, A. W. Glaetzle, R. Nath, and I. Lesanovsky, “Parallel execution of quantum gates in a long linear ion chain via Rydberg mode shaping”, *Phys. Rev. A* **87**, 052304 (2013).
- [44] M. Müller, L. Liang, I. Lesanovsky, and P. Zoller, “Trapped Rydberg ions: from spin chains to fast quantum gates”, *New Journal of Physics* **10**, 093009 (2008).

- [45] D. Jaksch, J. I. Cirac, P. Zoller, S. L. Rolston, R. Côté, and M. D. Lukin, “Fast quantum gates for neutral atoms”, *Physical Review Letters* **85**, 2208 (2000).
- [46] L. Isenhower, E. Urban, X. L. Zhang, A. T. Gill, T. Henage, T. A. Johnson, T. G. Walker, and M. Saffman, “Demonstration of a neutral atom controlled-nOT quantum gate”, *Physical Review Letters* **104**, 010503 (2010).
- [47] T. Wilk, A. Gaëtan, C. Evellin, J. Wolters, Y. Miroshnychenko, P. Grangier, and A. Browaeys, “Entanglement of two individual neutral atoms using rydberg blockade”, *Physical Review Letters* **104**, 010502 (2010).
- [48] I. S. Madjarov, J. P. Covey, A. L. Shaw, J. Choi, A. Kale, A. Cooper, H. Pichler, V. Schkolnik, J. R. Williams, and M. Endres, “High-fidelity entanglement and detection of alkaline-earth Rydberg atoms”, *Nature Physics* **16**, 857–861 (2020).
- [49] A. Omran, *et al.*, “Generation and manipulation of Schrödinger cat states in Rydberg atom arrays”, *Science* **365**, 570–574 (2019).
- [50] C. Zhang, F. Pokorny, W. Li, G. Higgins, A. Pöschl, I. Lesanovsky, and M. Hennrich, “Submicrosecond entangling gate between trapped ions via Rydberg interaction”, *Nature* **580**, 345–349 (2020).
- [51] A. G. Fowler, M. Mariantoni, J. M. Martinis, and A. N. Cleland, “Surface codes: Towards practical large-scale quantum computation”, *Physical Review A - Atomic, Molecular, and Optical Physics* **86**, 032324 (2012).
- [52] M. Saffman, “Quantum computing with atomic qubits and Rydberg interactions: Progress and challenges”, *J. Phys. B: At. Mol. Opt. Phys.* **49**, 202001 (2016).
- [53] T. Feldker, P. Bachor, M. Stappel, D. Kolbe, R. Gerritsma, J. Walz, and F. Schmidt-Kaler, “Rydberg Excitation of a Single Trapped Ion”, *Physical Review Letters* **115**, 173001 (2015).
- [54] G. Higgins, W. Li, F. Pokorny, C. Zhang, F. Kress, C. Maier, J. Haag, Q. Bordart, I. Lesanovsky, and M. Hennrich, “Single Strontium Rydberg Ion Confined in a Paul Trap”, *Physical Review X* **7**, 021038 (2017).
- [55] G. Higgins, F. Pokorny, C. Zhang, and M. Hennrich, “Highly Polarizable Rydberg Ion in a Paul Trap”, *Phys. Rev. Lett.* **123**, 153602 (2019).

- [56] S. Earnshaw *Earnshaw theorem*, 97th ed., Vol. 7 (Trans. Camb. Phil. Soc., 1874) pp. 97–112.
- [57] W. Paul and H. Steinwedel, “Notizen: Ein neues Massenspektrometer ohne Magnetfeld”, *Zeitschrift für Naturforschung A* **8**, 448–450 (1953).
- [58] L. S. Brown and G. Gabrielse, “Geonium theory: Physics of a single electron or ion in a Penning trap”, *Reviews of Modern Physics* **58**, 233 (1986).
- [59] R. D. Knight, “Storage of ions from laser-produced plasmas”, *Applied Physics Letters* **38**, 221–223 (1981).
- [60] J. E. Fulford, D. Nhu-Hoa, R. J. Hughes, R. E. March, R. F. Bonner, and G. J. Wong, “Radio-frequency mass selective excitation and resonant ejection of ions in a three-dimensional quadrupole ion trap”, *Journal of Vacuum Science and Technology* **17**, 829 (1980).
- [61] C. Zhang, *Fast and scalable entangling gate in trapped ions via Rydberg interaction* Ph.D. thesis, Stockholm University (2020).
- [62] D. J. Berkeland, J. D. Miller, J. C. Bergquist, W. M. Itano, and D. J. Wineland, “Minimization of ion micromotion in a Paul trap”, *Journal of Applied Physics* **83**, 5025–5033 (1998).
- [63] J. Eschner, G. Morigi, F. Schmidt-Kaler, and R. Blatt, “Laser cooling of trapped ions”, *Journal of the Optical Society of America B* **20**, 1003–1015 (2003).
- [64] D. Steck *Quantum and Atom Optics* (2007)  
Available at: <https://atomoptics.uoregon.edu/~dsteck/teaching/quantum-optics/>.
- [65] D. James, “Quantum dynamics of cold trapped ions with application to quantum computation”, *Applied Physics B: Lasers and Optics* **66**, 181–190 (1998).
- [66] J. Dalibard and C. Cohen Tannoudji, “Laser cooling below the Doppler limit by polarization gradients: simple theoretical models”, *Journal of The Optical Society of America B* **6**, 2023–2045 (1989).
- [67] P. J. Ungar, D. S. Weiss, E. Riis, and S. Chu, “Optical molasses and multilevel atoms: theory”, *Journal of The Optical Society of America B* **6**, 2058–2071 (1989).

- [68] D. Nigg, *Towards fault tolerant quantum computation* Ph.D. thesis, University of Innsbruck (2016).
- [69] H. Haffner, S. Gulde, M. Riebe, G. Lancaster, C. Becher, J. Eschner, F. Schmidt-Kaler, and R. Blatt, “Precision Measurement and Compensation of Optical Stark Shifts for an Ion-Trap Quantum Processor”, *Physical Review Letters* **90**, 143602 (2003).
- [70] S. H. Autler and C. H. Townes, “Stark Effect in Rapidly Varying Fields”, *Physical Review* **100**, 703–722 (1955).
- [71] C. Roos, *Controlling the quantum state of trapped ions* Ph.D. thesis, University of Innsbruck (2001).
- [72] E. Jaynes and F. Cummings, “Comparison of quantum and semiclassical radiation theories with application to the beam maser”, *Proceedings of the IEEE* **51**, 89–109 (1963).
- [73] J. Larson and T. Mavrogordatos, *The Jaynes–Cummings Model and Its Descendants: Modern research directions* (IOP Publishing, 2021).
- [74] G. Higgins, *A single trapped Rydberg ion* Ph.D. thesis, Stockholm University (2018).
- [75] F. Schmidt-Kaler, T. Feldker, D. Kolbe, J. Walz, M. Müller, P. Zoller, W. Li, and I. Lesanovsky, “Rydberg excitation of trapped cold ions: A detailed case study”, *New Journal of Physics* , 075014 (2011).
- [76] T. M. Graham, M. Kwon, B. Grinkemeyer, Z. Marra, X. Jiang, M. T. Lichtman, Y. Sun, M. Ebert, and M. Saffman, “Rydberg mediated entanglement in a two-dimensional neutral atom qubit array”, *Physical Review Letters* **123**, 230501 (2019).
- [77] H. Levine, A. Keesling, A. Omran, H. Bernien, S. Schwartz, A. S. Zibrov, M. Endres, M. Greiner, V. Vuletić, and M. D. Lukin, “High-fidelity control and entanglement of Rydberg atom qubits”, *Physical Review Letters* **121**, 123603 (2018).
- [78] H. Levine, *et al.*, “Parallel implementation of high-fidelity multi-qubit gates with neutral atoms”, *Physical Review Letters* **123**, 170503 (2019).
- [79] B. Bransden and C. Joechain *Physics of atoms and molecules* (1983).

- [80] A. D. Ludlow, M. M. Boyd, J. Ye, E. Peik, and P. O. Schmidt, “Optical atomic clocks”, *Rev. Mod. Phys.* **87**, 637 (2015).
- [81] J. Walz, I. Siemers, M. Schubert, W. Neuhauser, R. Blatt, and E. Teloy, “Ion storage in the rf octupole trap”, *Physical Review A* **50**, 4122 (1994).
- [82] T. Schaetz, “Trapping ions and atoms optically”, *Journal of Physics B: Atomic, Molecular and Optical Physics* **50**, 102001 (2017).
- [83] L. Karpa, *Trapping Single Ions and Coulomb Crystals with Light Fields* (Springer International Publishing, 2019).
- [84] G. Barwood, H. Margolis, G. Huang, P. Gill, and H. Klein, “Measurement of the Electric Quadrupole Moment of the  $4d\ D\ 5/2\ 2$  Level in  $Sr^{+88}$ ”, *Physical review letters* **93**, 133001 (2004).
- [85] C. F. Roos, D. Leibfried, A. Mundt, F. Schmidt-Kaler, J. Eschner, and R. Blatt, “Experimental Demonstration of Ground State Laser Cooling with Electromagnetically Induced Transparency”, *Physical Review Letters* **85**, 5547–5550 (2000).
- [86] R. Lechner, C. Maier, C. Hempel, P. Jurcevic, B. P. Lanyon, T. Monz, M. Brownnutt, R. Blatt, and C. F. Roos, “Electromagnetically-induced-transparency ground-state cooling of long ion strings”, *Physical Review A* **93**, 053401 (2016).
- [87] F. Pokorny, C. Zhang, G. Higgins, and M. Hennrich, “Magic trapping of a Rydberg ion with a diminished static polarizability”, [arXiv:2005.12422](https://arxiv.org/abs/2005.12422) (2020), [10.48550/arXiv.2005.12422](https://arxiv.org/abs/2005.12422).
- [88] A. Pöschl, *Laser ablation loading and single ion addressing of Strontium in a linear Paul trap* Master’s thesis, Stockholm University (2018).
- [89] A. Lindberg, *Improving the coherent control of trapped ion qubits* Master’s thesis, Stockholm University (2020).
- [90] F. Pokorny, *A microwave dressed Rydberg ion* Ph.D. thesis, Stockholm University (2020).
- [91] C. Maier, *Laser system for the Rydberg excitation of Strontium ions* Master’s thesis, University of Innsbruck (2013).
- [92] R. W. P. Drever, J. L. Hall, F. V. Kowalski, J. Hough, G. M. Ford, A. J.

- Munley, and H. Ward, “Laser phase and frequency stabilization using an optical resonator”, *Applied Physics B: Lasers and Optics* **31**, 97 (1983).
- [93] E. Jansson, *Frequency stabilization of a laser at 674nm for coherent manipulation of Strontium-88 ions* Master’s thesis, Stockholm University (2020).
- [94] H. Parke, *et al.*, “Phononic bright and dark states: Investigating multi-mode light-matter interactions with a single trapped ion”, *arXiv:2403.07154* (2024), 10.48550/arXiv.2403.07154.
- [95] M. Mallweger, M. H. de Oliveira, R. Thomm, H. Parke, N. Kuk, G. Higgins, R. Bachelard, C. J. Villas-Boas, and M. Hennrich, “Single-Shot Measurements of Phonon Number States Using the Autler-Townes Effect”, *Phys. Rev. Lett.* **131**, 223603 (2023).
- [96] M. Mallweger, M. Guevara-Bertsch, B. T. Torosov, R. Thomm, N. Kuk, H. Parke, C. F. Roos, G. Higgins, M. Hennrich, and N. V. Vitanov, “Motional-state analysis of a trapped ion by ultranarrowband composite pulses”, *Phys. Rev. A* **110**, 053103 (2024).
- [97] C. W. Chou, A. L. Collopy, C. Kurz, Y. Lin, M. E. Harding, P. N. Plessow, T. Fortier, S. Diddams, D. Leibfried, and D. R. Leibbrandt, “Frequency-comb spectroscopy on pure quantum states of a single molecular ion”, *Science* **367**, 1458–1461 (2020).
- [98] S. M. Brewer, J.-S. Chen, A. M. Hankin, E. R. Clements, C. W. Chou, D. J. Wineland, D. B. Hume, and D. R. Leibbrandt, “ $^{27}\text{Al}^+$  Quantum-Logic Clock with a Systematic Uncertainty below  $10^{-18}$ ”, *Phys. Rev. Lett.* **123**, 033201 (2019).
- [99] G. Higgins, C. Zhang, F. Pokorny, H. Parke, E. Jansson, S. Salim, and M. Hennrich, “Observation of second- and higher-order electric quadrupole interactions with an atomic ion”, *Physical Review Research* **3**, L032032 (2021).
- [100] G. Higgins, S. Salim, C. Zhang, H. Parke, F. Pokorny, and M. Hennrich, “Micromotion minimization using Ramsey interferometry”, *New Journal of Physics* **23**, 123028 (2021).
- [101] T. Gallagher and W. Cooke, “Interactions of blackbody radiation with atoms”, *Physical Review Letters* **42**, 835 (1979).
- [102] R. Alheit, K. Enders, and G. Werth, “Isotope separation by nonlinear reso-

- nances in a Paul trap”, *Applied Physics B* **62**, 511–513 (1996).
- [103] T. Hasegawa and T. Shimizu, “Removal of irrelevant isotope ions in the presence of laser cooling in a rf trap”, *Applied Physics B* **70**, 867–871 (2000).
- [104] J. Andrijauskas, J. Vogel, A. Mokhberi, and F. Schmidt-Kaler, “Rydberg Series Excitation of a Single Trapped  $^{40}\text{Ca}^+$  Ion for Precision Measurements and Principal Quantum Number Scalings”, *Phys. Rev. Lett.* **127**, 203001 (2021).
- [105] C. D. Bruzewicz, R. McConnell, J. Chiaverini, and J. M. Sage, “Scalable loading of a two-dimensional trapped-ion array”, *Nature communications* **7**, 13005 (2016).
- [106] R. J. Niffenegger, *et al.*, “Integrated multi-wavelength control of an ion qubit”, *Nature* **586**, 538–542 (2020)